FISEVIER

Contents lists available at ScienceDirect

# Journal of Alloys and Compounds

journal homepage: www.elsevier.com/locate/jalcom



# Novel Ti-Zr-Hf-Nb-Fe refractory high-entropy alloys for potential biomedical applications



Wenjie Wang<sup>a,c</sup>, Kaihuai Yang<sup>b</sup>, Qianting Wang<sup>a,c</sup>, Pinqiang Dai<sup>a,c</sup>, Hui Fang<sup>a,c</sup>, Fangjuan Wu<sup>a,c</sup>, Qiaohang Guo<sup>a,c</sup>, Peter K. Liaw<sup>d</sup>, Nengbin Hua<sup>a,c,\*</sup>

- <sup>a</sup> Department of Materials Science and Engineering, Fujian University of Technology, 350118 Fuzhou, China
- <sup>b</sup> School of Mechanical and Intelligent Manufacturing, Fujian Chuanzheng Communications College, 350007 Fuzhou, China
- <sup>c</sup> Fujian Provincial Key Laboratory of Advanced Materials Processing and Application, Fujian University of Technology, 350118 Fuzhou, China
- <sup>d</sup> Department of Materials Science and Engineering, the University of Tennessee, 37996-2200 Knoxville, TN, USA

#### ARTICLE INFO

#### Article history: Received 18 January 2022 Received in revised form 23 February 2022 Accepted 25 February 2022 Available online 26 February 2022

Keywords: Metallic biomaterials High-entropy alloys Mechanical properties Corrosion Wear

#### ABSTRACT

In the present work, the TiZrHfNbFe $_x$  (x = 0, 0.25, 0.5, 0.75, 1, 1.5, and 2, molar ratio) refractory high-entropy alloys (HEAs) were developed. The microstructure, mechanical properties, corrosion and wear resistance of the Ti-Zr-Hf-Nb-Fe HEAs were investigated. The Ti-Zr-Hf-Nb-Fe HEAs exhibited a dendrite structure with body-centered-cubic (BCC) + Laves phases. Among them, the TiZrHfNbFe $_{0.5}$  HEA displayed good comprehensive mechanical properties with the hardness of 420 HV, compressive strength of 1450 MPa, and plastic strain of about 8%. In addition, the TiZrHfNbFe $_{0.5}$  HEA possessed better corrosion resistance than that of the Ti6Al4V and the other Ti-Zr-Hf-Nb-Fe HEAs in phosphate buffer saline (PBS) solution, which might be related to the generation of more protective oxide films on its surface. Furthermore, the wear resistance of the Ti-Zr-Hf-Nb-Fe HEAs increased with the raise of the Fe content. The TiZrHfNbFe $_{0.5}$  HEA demonstrated superior dry and wet wear resistance in comparison with the Ti6Al4V alloy. Therefore, the good mechanical properties, high corrosion, and wear resistance, the biocompatible constituent elements, as well as the low cost of the Fe addition render the Ti-Zr-Hf-Nb-Fe HEAs as promising candidates as biomedical-implantation materials

© 2022 Elsevier B.V. All rights reserved.

#### 1. Introduction

In recent years, biomaterials, which include biomedical metals, ceramics, and polymers, have become a hot spot in the material research [1,2]. Owing to the superior combination of strength and plasticity, metallic materials exhibit superior advantages in the applications of biomedical implant materials, such as orthopedics bone plates, dental roots, artificial hip joints, and cardiovascular stents [3]. Currently, Ti-based alloys, Co-Cr-based alloys, and 316L stainless steels are the major metallic implant materials in a clinic [4]. Among those, the Ti-based alloys showing good biocompatibility, high corrosion resistance, and specific strength to density, have been widely used as dental and orthopedic implants. However, due to the low wear resistance of Ti-based alloys, "particle diseases" resulted from the wear debris may occur when they are performing under the physiological environments [5,6]. The Co-Cr-based alloys possess

E-mail address: flower1982cn@126.com (N. Hua).

high strength and superior wear resistance, which makes them the first choice of hip joints for frictional surfaces [7]. Nevertheless, during the long-term service of Co-Cr-based alloys in the human body, the release of toxic Co and Cr ions may cause necrosis of surrounding tissues and even tumors, which restricts their extensive biomedical applications [4,8].

After conventional biomedical alloys have been implanted, frictional wear is usually accelerated by corrosive physiological fluids, leading to a greater amount of material loss, which is corrosive wear [9], which may seriously reduce the service longevity. Thus, the excellent biocompatibility, high corrosion resistance, and good wear resistance are all essential for biomedical metallic-implant alloys. The development of novel implant biometals with good comprehensive properties, especially the high corrosive-wear resistance, is of great scientific significance and clinical application value.

Yeh and Cantor et al. proposed the concept of high-entropy alloys (HEAs) or multicomponent alloys in 2004, respectively [10,11]. Unlike traditional alloys, HEAs are those consisting five or more metallic elements in equimolar or near-equimolar ratios, which possess the following four core effects: high entropy, lattice distortion,

<sup>\*</sup> Correspondence to: School of Materials Science and Engineering, Fujian University of Technology, Fuzhou 350118, China.

sluggish diffusion, and 'cocktail' effects [12,13]. These effects can change the microstructure of HEAs, granting them greater mechanical properties and corrosion resistance than those of conventional 2-element or 3-element alloys [14,15]. In the past decades, various HEA systems, such as transitional element HEAs [16,17], refractory HEAs [18,19], high-entropy metallic glasses [20], eutectic HEAs [21–23], have been successfully fabricated. Furthermore, owing to the high biocompatibility of constituent elements of the Ti-Zr-Nb-based refractory HEAs, their prospect in the biomedical application has attracted extensive attention. Several biocompatible systems, including the Ti-Zr-(Hf, Nb, Ta) [24], Hf-Nb-Ti-Zr [25], Ti-Zr-Nb-Ha [26], Ti-Zr-Nb-Mo-Ta [27,28], Ti-Zr-Nb-Hf-Ta [29,30], Ti-Zr-Nb-Hf-Mo [31], Ti-Zr-Nb-Cu-Ag [32], Ti-Ni-Cr-Fe-Co [33], and Ti-Zr-Hf-Nb-Ta-Mo [34,35] HEAs, have been developed.

The Ti-Zr-Nb-based refractory HEAs generally show the bodycentered-cubic (BCC) solid solution structures, and thus, exhibit the higher hardness, yield strength, and wear resistance than those of the Ti6Al4V alloy. The high strength renders them great tolerance to plastic deformation and fracture under high loads. The high hardness of the HEAs may decrease the possibility of the "particle disease" when working in the physiological environment as stressbearing implant materials [27,28,36]. Moreover, it has been reported that the refractory metallic elements of Ti-Zr-Nb-based refractory HEAs were prone to form a greatly-protective dense oxide surface layer, and thus, possessed good corrosion resistance [14,37,38]. It was found that the MC3T3-E1 pre-osteoblasts on the equiatomic and non-equiatomic TiZrHfNbTa HEA showed good adhesion, viability, and proliferation behaviors [37,39]. The hydroxyapatite (HA) formation was evident on the surfaces of the TiTaHfNb, TiTaHfNbZr and TiTaHfMoZr HEAs when they were subjected to static immersion experiments in fetal bovine serum (FBS) media, indicating their great potential for utility in orthopedic implants [40]. To sum up, the Ti-Zr-Nb-based HEAs display better comprehensive properties than those of traditional biomedical materials, and demonstrate promising potential in the biomedical applications [27,28,30].

To date, researchers have developed various Ti-Zr-Nb-based HEA systems, but most of their constituent elements are in equimolar ratios. The microstructures and properties of HEAs were affected by changing the content of constituent elements. For instance, the Ti<sub>0.5</sub>ZrNbTaMo HEA showed higher yield strength and wear resistance than those of the equimolar TiZrNbTaMo HEA [41]. Moreover, the Ti<sub>1.5</sub>ZrTa<sub>0.5</sub>Hf<sub>0.5</sub>Nb<sub>0.5</sub> HEA exhibited similar hardness and higher corrosion resistance in comparison with those of the TiZr-TaHfNb HEA [36]. As a result, it is necessary to investigate the impact of alloying elements on the microstructures, mechanical properties, corrosion and wear behaviors of HEAs in a systematic way. It was found that the TiZrHfNb refractory HEA presented a good plasticdeformation ability, but a low yield strength and poor wear resistance [25]. Moreover, for the Ti-Zr-Nb-Ta-Mo/Hf HEAs, the Ta and Mo constituent elements possess ultra-high melting points and high cost, which limit their wide applications.

In this paper, novel Ti-Zr-Hf-Nb-Fe HEAs were developed for the first time by alloying a low toxic Fe element into the Ti-Zr-HfNb alloy. Compared with the Ti-Zr-Nb-Ta-Mo and Ti-Zr-Hf-Nb-Ta refractory alloys, the Ti-Zr-Hf-Nb-Fe HEAs exhibited a lower melting point and a reduced cost of raw materials. Hence, we systematically studied the effects of the Fe addition on the microstructures and properties of the Ti-Zr-Nb-based HEAs for future biomedical applications.

## 2. Methodology

#### 2.1. Sample preparation

The Ti, Zr, Hf, Nb, and Fe raw materials with high purity were mixed according to the nominal compositions of TiZrHfNbFe $_x$  (x = 0, 0.25, 0.5, 0.75, 1, 1.5, and 2, molar ratio), which were denoted as Fe $_0$ ,

Fe $_{0.25}$ , Fe $_{0.75}$ , Fe $_{1.75}$ , Fe $_{1.5}$ , and Fe $_{2}$ , respectively, for abbreviation. The master alloy ingots were arc-melted under a high-purity argon atmosphere. All of these ingots were repeatedly melted for at least five times to ensure a uniform distribution of the constituent components. All rod (2 × 2 × 4 mm³) and sheet (3 × 3 × 2 mm³ and 10 × 10 × 2 mm³) samples were cut from the middle area of the ingots by wire-cut electrical-discharge machining (WEDM). The surface of the alloy specimen was polished after grinding with 240–5000 grit silicon carbide sandpaper.

#### 2.2. Structure characterization

The Bruker-AXS-D8 X-ray diffractometer (XRD) was used to characterize the crystal structure of the alloys using a monochromatic Cu target  $K\alpha$ -rays at 40 kV and 40 mA with a scanning range, 20, of 20–80° at a scanning rate of 2°/min. The surface morphology of the samples was analyzed by an S-3400N scanning electron microscope (SEM), and the accompanying energy dispersive spectrometer (EDS) was used for compositional analysis.

#### 2.3. Mechanical property tests

The room-temperature compressive deformation test was conducted, using a Shimadzu AGS-X type mechanical-testing system (MTS), and the strain rate was  $2.1 \times 10^{-4} \, \rm s^{-1}$ . The specimen geometry for the compression experiment was about  $2 \times 2 \times 4 \, \rm mm^3$ . The fracture surface after the compression test were observed by SEM. A THV-10D Vickers hardness tester was used to complete the microhardness test with a load of 300 gf and a dwell time of 15 s. At least five points per sample were examined to ensure reproducibility.

#### 2.4. Corrosion experiments

Electrochemical tests were performed on the HEAs in the phosphate buffer saline (PBS) solution by an electrochemical workstation. The samples were embedded in an epoxy resin and connected to a copper wire. The surfaces of the specimens were polished with a silicon-carbide sandpaper up to 5000 grit, followed by ultrasonic cleaning in acetone, ethanol, and deionized water, respectively, and air-drying. In this study, a Pt-plate counter electrode and a saturated calomel reference electrode (SCE), together with a specimen (working electrode), formed a three-electrodes system. The potentiodynamic-polarization experiments were carried out, using the three-electrodes system in the PBS solution. At last, the surface morphologies were observed by SEM, and the compositional distribution of corroded samples was examined by EDS.

#### 2.5. Surface-chemistry analysis

The ESCALab250Xi X-ray photoelectron spectrometer (XPS) was used to further investigate the composition and structure of the surface passive film of the HEAs, which had been immersed in the PBS solution for 24 h. The full spectra of the HEAs and narrow scan spectra of the Ti 2p, Zr 3d, Hf 4f, Nb 3d, Fe 3d, and O 1s were examined.

# 2.6. Wear experiments

The HSR-2M reciprocating-type sliding tester was used to study the friction and wear behavior of Ti-Zr-Hf-Nb-Fe HEAs for, and a  $Si_3N_4$  ball (6 mm in diameter) was employed as the couple pair. The parameters of the wear test in this study were set as follows: a normal load of 5 N, a friction time of 30 min, a sliding frequency of 60 rpm, and a sliding stroke of 5 mm. The friction coefficient was recorded during the sliding process, and the MT-500 probe-type material surface profile measuring instrument was used to

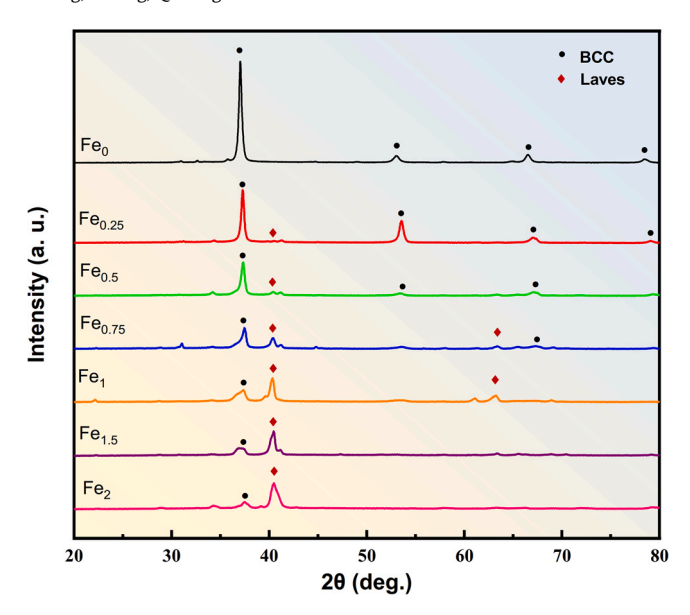


Fig. 1. XRD pattern of the Ti-Zr-Hf-Nb-Fe HEAs.

determine the wear volume of the HEAs. The wear-scar morphology of the worn surface was investigated by SEM. The surface composition was analyzed by EDS.

#### 3. Results

#### 3.1. Phase analysis and morphology observation of the HEAs

Fig. 1 shows the XRD diffraction patterns of the Ti-Zr-Hf-Nb-Fe HEAs. The XRD pattern of the Fe0 alloy reveals only one single body-centered-cubic (BCC) solid-solution phase. Meanwhile, a new tiny diffraction peak appears near 41° on the XRD pattern of the Fe $_{0.25}$  alloy, which is verified as the Laves (Fe $_{2}$ Nb) phase. Moreover, the intensity of the diffraction peak around 38° in accordance with the BCC phase significantly decreases with the Fe-element addition, demonstrating that the structure of the TiZrHfNb HEA gradually changes from a single BCC phase structure to the BCC and Laves phases mixed structure due to the addition of Fe. With the further increase in the Fe content, the diffraction peak intensity of the Laves phase gradually increases, and that of the BCC phase decreases, the fraction of the Laves phase even exceeds that of the BCC phase and becomes the main phase for the Fe $_{1}$ , Fe $_{1.5}$ , and Fe $_{2}$  alloys.

As presented in Fig. 1, owing to the addition of the Fe element, the diffraction peaks referring to the BCC phase slightly shift to the higher  $2\theta$  angle, while the peaks representing the Laves phase broaden. The Bragg equation states:

$$2d\sin\theta = n\lambda \tag{1}$$

where the d,  $\theta$ , and  $\lambda$  are the interplanar distance, the diffraction angle, and the X-ray wavelength, respectively. The peak shift of the BCC phase may result from the substitution of Fe with a smaller atomic radius for Ti, Zr, Hf, and Nb elements with larger atomic radii, which leads to the shrink of the crystal cell, the decrease in the crystal plane spacing, and eventually the lattice distortion. The Scherrer's formula has been proposed as follows:

$$D = \frac{K\lambda}{B\cos\theta} \tag{2}$$

where K is the Scherrer constant, D is the average crystal size, B is the full width at half maximum (FWHM) intensity of the peak,  $\theta$  is the diffraction angle, and  $\lambda$  is the X-ray wavelength. Accordingly, the broadening of diffraction peaks for the Laves phase may be due to

the grain refinement by the addition of Fe.

Zhang et al. [42,43] proposed a criterion for the solid-solution-phase formation based on the mixing enthalpy ( $\Delta H_{\text{mix}}$ ) and atomic-radius difference ( $\delta_{\text{r}}$ ) to predict the structural stability and phase formation of HEAs. We can state the  $\Delta H_{\text{mix}}$  and  $\delta_{\text{r}}$  as follows:

$$\Delta H_{mix} = 4 \sum_{i=1, i \neq j}^{n} \Delta H_{ij}^{mix} c_i c_j \tag{3}$$

$$\delta_r = \sqrt{\sum_{i=1}^n c_i (1 - r_i/\bar{r})^2} \cdot 100\%$$
(4)

where  $\Delta H^{\text{mix}}$  <sup>ij</sup>is the mixing enthalpy of the *i*-th and *j*-th alloying elements,  $c_i$  and  $c_j$  represent the atomic percents (at%) of the *i*-th and *j*-th alloying elements,  $r_i$  is the atomic radius of the *i*-th element, and  $\bar{r}$  is the average atomic radius of the alloy. A negative  $\Delta H_{\text{mix}}$  tends to combine different elements into intermetallic compounds, and the more negative  $\Delta H_{\text{mix}}$  is, the greater bonding force between different elements. However, the more positive  $\Delta H_{\text{mix}}$  is, the lower miscibility of different elements in the alloy, which leads to the chemical separation or segregation. Only when the value of  $\Delta H_{\text{mix}}$  is close to 0, the different elements can be randomly distributed in the alloy and form a stable solid-solution phase. In addition, to further consider the mixing entropy ( $\Delta S_{\text{mix}}$ ) effect, a new parameter, " $\Omega$ ", has been proposed as [43]:

$$\Omega = \frac{T_m \Delta S_{mix}}{|\Delta H_{mix}|} \tag{5}$$

$$\Delta S_{mix} = -R \sum_{i=1}^{n} (c_i \ln c_i)$$
(6)

where  $T_{\rm m}$  is the average melting temperature, R is the gas constant.  $\Omega \geq 1.1$  and  $\delta_{\rm r} \leq 6.6\%$  are necessary for forming the solid-solution phases, and the smaller the  $\Omega$  or the larger the  $\delta_{\rm r}$ , the easier it is to form intermetallics phases [43]. The thermodynamic parameters and the atomic-radius differences of the Ti-Zr-Hf-Nb-Fe alloy are summarized in Table 1. The  $\Omega$  and  $\delta_{\rm r}$  of the Fe $_{\rm 0}$  alloy are 10.75% and 4.26%, respectively, which results in forming a stable BCC solid-solution phase. Moreover, the Fe $_{\rm 0.25}$  alloy shows a  $\delta_{\rm r}$  value of 6.67% slightly higher than critical value of 6.6%, and thus forms a small amount of intermetallics. As the Fe fraction further rises, the values of  $\Omega$  gradually decreases, and  $\delta_{\rm r}$  increases, which is favorable for the formation of intermetallics. Accordingly, increasing the Fe content in the Ti-Zr-Hf-Nb-Fe HEAs results in the enrichment of the Laves phase and depletion of the BCC phase, which is consistent with the XRD result in Fig. 1.

The surface morphologies of the Ti-Zr-Hf-Nb-Fe HEAs are shown in Fig. 2. In Fig. 2(a), it can be observed that the Fe<sub>0</sub> alloy shows a homogeneous structure morphology, and the EDS analysis also proves the uniform distribution of constituent elements of Ti, Zr, Hf, and Nb. Furthermore, the microstructures of the Ti-Zr-Hf-Nb-Fe HEAs are composed of the dendrites and interdendrites. They are illustrated by the light gray and dark gray contrast areas, respectively. As the fraction of the Fe element increases, the microstructures of the HEAs change significantly, the arms of dendrites

**Table 1**  $\Delta H_{\rm mix}$ ,  $\delta_{\rm r}$ ,  $\Delta S_{\rm mix}$ ,  $\Omega$ , and  $T_{\rm m}$  of the Ti-Zr-Hf-Nb-Fe HEAs.

	$\Delta H_{ m mix}$	$\delta_{ m r}$	$\Delta S_{\rm mix}$	Ω	$T_{\rm m}$ (K)
Fe <sub>0</sub>	2.5	4.26%	11.53	10.75	2331.25
$Fe_{0.25}$	-2.25	6.67%	12.79	13.01	2300.65
Fe <sub>0.5</sub>	-5.71	7.25%	13.10	5.16	2273.44
Fe <sub>0.75</sub>	-8.85	7.87%	13.34	3.39	2249.11
Fe <sub>1</sub>	-11.04	8.32%	13.38	2.70	2227.20
Fe <sub>1.5</sub>	-14.06	9.03%	13.20	2.04	2189.36
$Fe_2$	-16.57	9.65%	13.06	1.72	2157.83

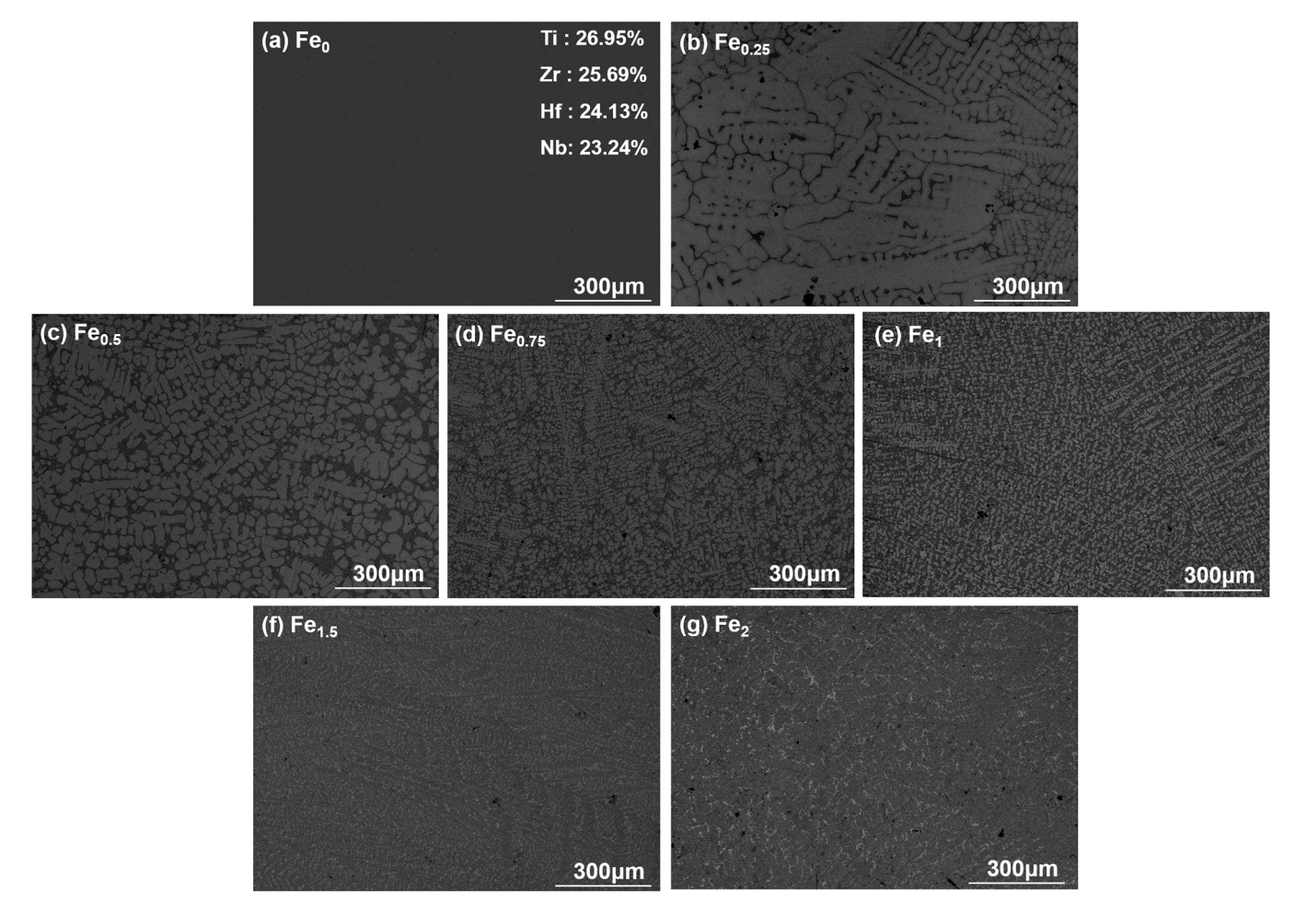
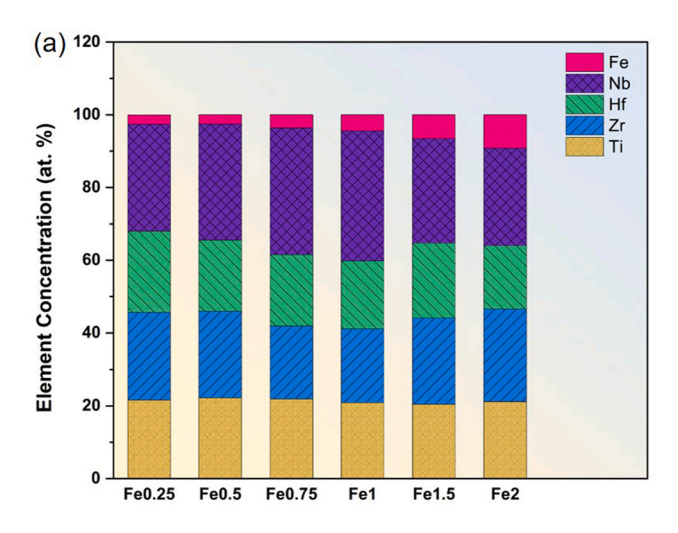


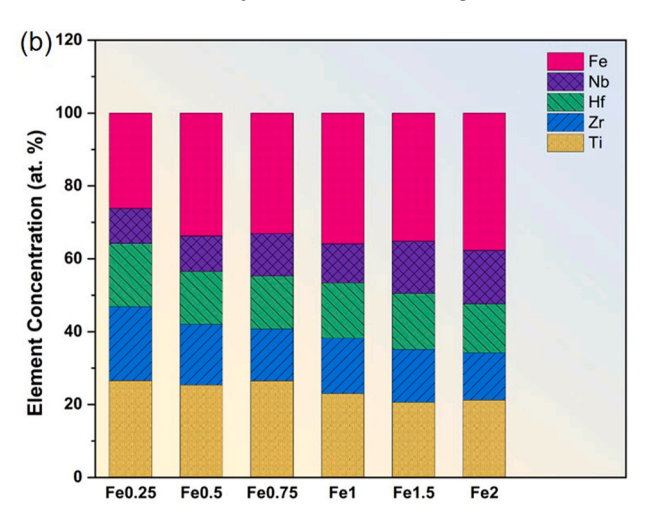
Fig. 2. SEM images of the surface morphologies for the Ti-Zr-Hf-Nb-Fe HEAs.

become thinner and shorter, and the regions of interdendrites gradually increase. Typically, as seen in Fig. 2(e), the Fe $_1$  alloy presents a fine lamellar structure with a large amount of thin dendrite and interdendrite zones.

Fig. 3(a: dendrite, b: interdendrite) illustrates the compositional EDS results of constituent elements for the Ti-Zr-Hf-Nb-Fe HEAs. It is obvious that the Nb element is remarkably enriched, and the Fe element is depleted in the dendritic region of the HEAs. On the contrary, the Fe element is significantly enriched in the

interdendritic regions of the HEAs. Due to the varying melting points of various elements in the present HEAs, the inhomogeneous distributions of constituent elements take place in different regions [44]. Among those, Ti, Zr, Hf, and Nb exhibit high melting points of 1668 °C, 1855 °C, 2233 °C, and 2477 °C, respectively, while Fe possesses the lowest melting point of 1538 °C. During the solidification process of the HEAs, high-melting-point elements, such as Nb, are preferentially precipitated in the dendrites, while Fe is subsequently solidified and mainly distributed among the interdendrites.





 $\textbf{Fig. 3.} \ \ \text{EDS results of the Ti-Zr-Hf-Nb-Fe HEAs (a: dendrite, b: interdendrite)}.$ 

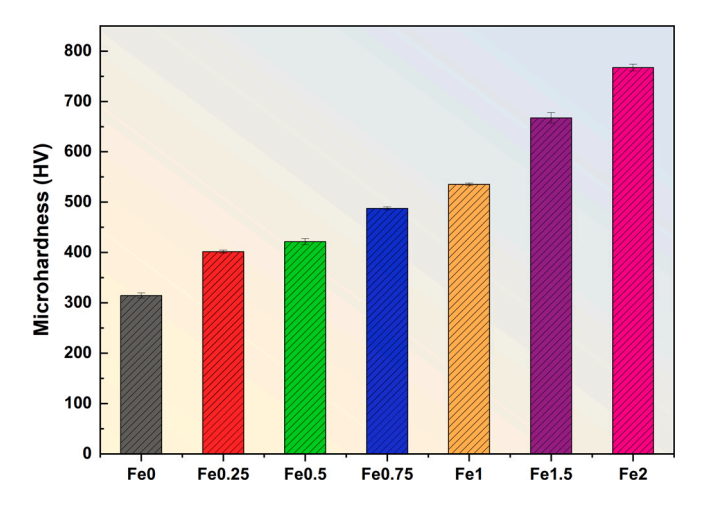


Fig. 4. Vickers microhardness of the Ti-Zr-Hf-Nb-Fe HEAs.

Therefore, as the fraction of Fe enhances, the dendrites in a gray contrast in Fig. 2 become finer, while the interdendrite region in a dark contrast gradually increases in size. Combined with the analysis of XRD and EDS, the dendritic phase is mainly the BCC phase, and the interdendritic phase corresponds to the Laves phase.

#### 3.2. Hardness and compression test of the HEAs

Fig. 4 exhibits the Vickers microhardness of the Ti-Zr-Hf-Nb-Fe HEAs. From Fig. 4, with the increase in the Fe element, the hardness values of the HEAs increase monotonically, which is mainly due to the increasing fraction of a hard Laves phase. The microhardness of the Fe $_{0.25}$  alloy is 400 HV, which is higher than the reported value of 320 HV for the Ti6Al4V alloy. It is worth mentioning that the microhardness of the Fe $_2$  alloy even reaches about 770 HV, which indicates that the Ti-Zr-Hf-Nb-Fe HEAs may possess good wear resistance.

Fig. 5 presents the compressive stress-strain curves of the Ti-Zr-Hf-Nb-Fe HEAs at room temperature. It is seen that the Fe $_0$  alloy shows a large compressive plastic strain up to 30%, and a moderate yield strength of  $\sim$  750 MPa. With the increase in the Fe content, the yield strength of the HEAs increases significantly from  $\sim$  750 MPa for the Fe $_0$  alloy to  $\sim$  1500 MPa for the Fe $_1$  alloy, but the plastic strain decreases from  $\sim$  30% to less than 2%. Further increasing the content of Fe, the strength of the HEA decreases, and the compressive strengths of the Fe $_1$ 5 and Fe $_2$  alloys are  $\sim$  1250 MPa and  $\sim$  180 MPa, respectively, showing obvious brittle fracture characteristics. The

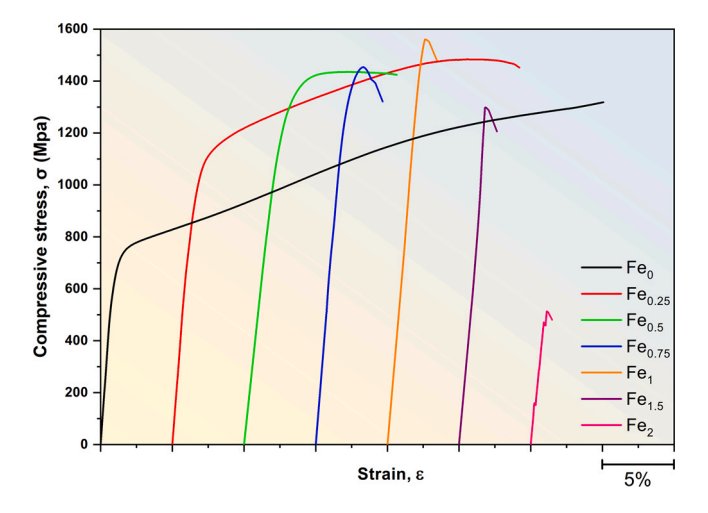


Fig. 5. Compressive stress-strain curves of the Ti-Zr-Hf-Nb-Fe HEAs.

Fe $_{0.25}$  and Fe $_{0.5}$  alloys possess good comprehensive mechanical properties, namely the strength-plasticity trade-off. The yield strength and plastic strain of the Fe $_{0.25}$  are  $\sim$  1100 MPa and  $\sim$  20%, respectively. The yield strength and plastic strain of the Fe $_{0.5}$  are  $\sim$  1450 MPa and  $\sim$  8%, respectively.

The mechanical properties of alloys are often related to their crystalline-phase structures and microstructures. As shown in Fig. 1, the HEAs change from the single BCC-phase structure to the dual BCC and Laves phases structure, as the fraction of Fe increases. Compared with the BCC phase, the Laves phase with the hexagonalclose-packed (HCP) structure displays less slip systems and basically does not undergo large plastic deformation, exhibiting the hard and brittle characteristics [45]. Therefore, the increasing amount of the Laves phase results in the improvement of yield strength and the deterioration of plasticity for the HEAs. As the Fe content exceeds 1, the embrittlement of the HEAs takes place, which is attributed to the significant enrichment of the Laves phase and the depletion of the BCC phase. In addition, the Fe<sub>0.25</sub> alloy has a large volume fraction of dendrites, and the dendrite arms are almost connected, as presented in Fig. 2. According to the previous study [46], the coarse dendritic structure in the HEAs usually shows the greater plasticity than that of the equiaxed fine dendritic structure. Therefore, the Fe<sub>0.25</sub> alloy exhibits a larger plastic-deformation capacity. Furthermore, as the content of Fe gradually increases, the dendrite arms become thinner and shorter, and the volume fraction of dendrites decreases, leading to a decrease in the plasticity of the HEAs as well.

The surface morphologies for the Ti-Zr-Hf-Nb-Fe HEAs after the compressive deformation are shown in Fig. 6, and the insets display their magnified morphologies. It can be seen from Fig. 6(a) that there are plenty of shear bands on the surface of the Fe<sub>0</sub> alloy (as indicated by white arrows), which verifies that the Fe<sub>0</sub> alloy exhibits a good plastic-deformation ability. With the increase in the Fe content, as presented in Fig. 6(b) and (c), the shear-band densities of the deformed HEA samples decrease, and a few cracks can be detected on the surfaces (as marked by white circles). The shear -band density of the Fe<sub>0.25</sub> is larger than that of the Fe<sub>0.5</sub>, demonstrating that the superior plasticity of the Fe<sub>0.25</sub> alloy. As illustrated in Fig. 6(d), there are no obvious shear bands on the surface of the deformed Fe<sub>0.75</sub> alloy. Moreover, it can be found that there are uneven cleavage steps and dimple-like microstructure morphologies on the fracture surface of the alloy. Furthermore, the Fe<sub>1</sub>, Fe<sub>1.5</sub>, and Fe<sub>2</sub> alloys exhibit river-like patterns on the smooth fracture surface without dimpleslike microstructures, confirming the brittle-fracture characteristic. As the content of Fe increases, the regions of the interdendrites expand, and the Fe<sub>2</sub>Nb phase is gradually coarsened. Accordingly, the HEAs become more prone to dislocation pile-up when subjected to load, which is one of the main reasons leading to the cleavage fracture. Therefore, raising the Fe content generally causes the drop of plasticity for the Ti-Zr-Hf-Nb-Fe HEAs.

#### 3.3. Electrochemical behavior of the Ti-Zr-Hf-Nb-Fe HEAs

Fig. 7 shows the potentiodynamic-polarization curves of the Ti-Zr-Hf-Nb-Fe HEAs in the PBS solution. Table 2 summarizes the relevant electrochemical parameters. With the increase in the Fe content ( $0 \le x \le 1$ ), the corrosion potential ( $E_{corr}$ ) of the alloy initially decreases from - 0.39 V for the Fe $_0$  alloy to - 0.42 V for the Fe $_{0.25}$  alloy, and subsequently increases to - 0.27 V for the Fe $_1$  alloy. The decrease in the corrosion potential of the Fe $_{0.25}$  alloy may be due to the appearance of the Laves phase in the alloy, which transforms the structure of HEAs from a single-phase structure to a dual-phase structure. The difference in compositions of two phases leads to the generation of galvanic corrosion [47,48], resulting in the decrease in the corrosion potential. Further increasing the Fe content enhances the corrosion potential of the HEAs, which is attributed to the refinement and homogenization of the microstructure. Moreover, the

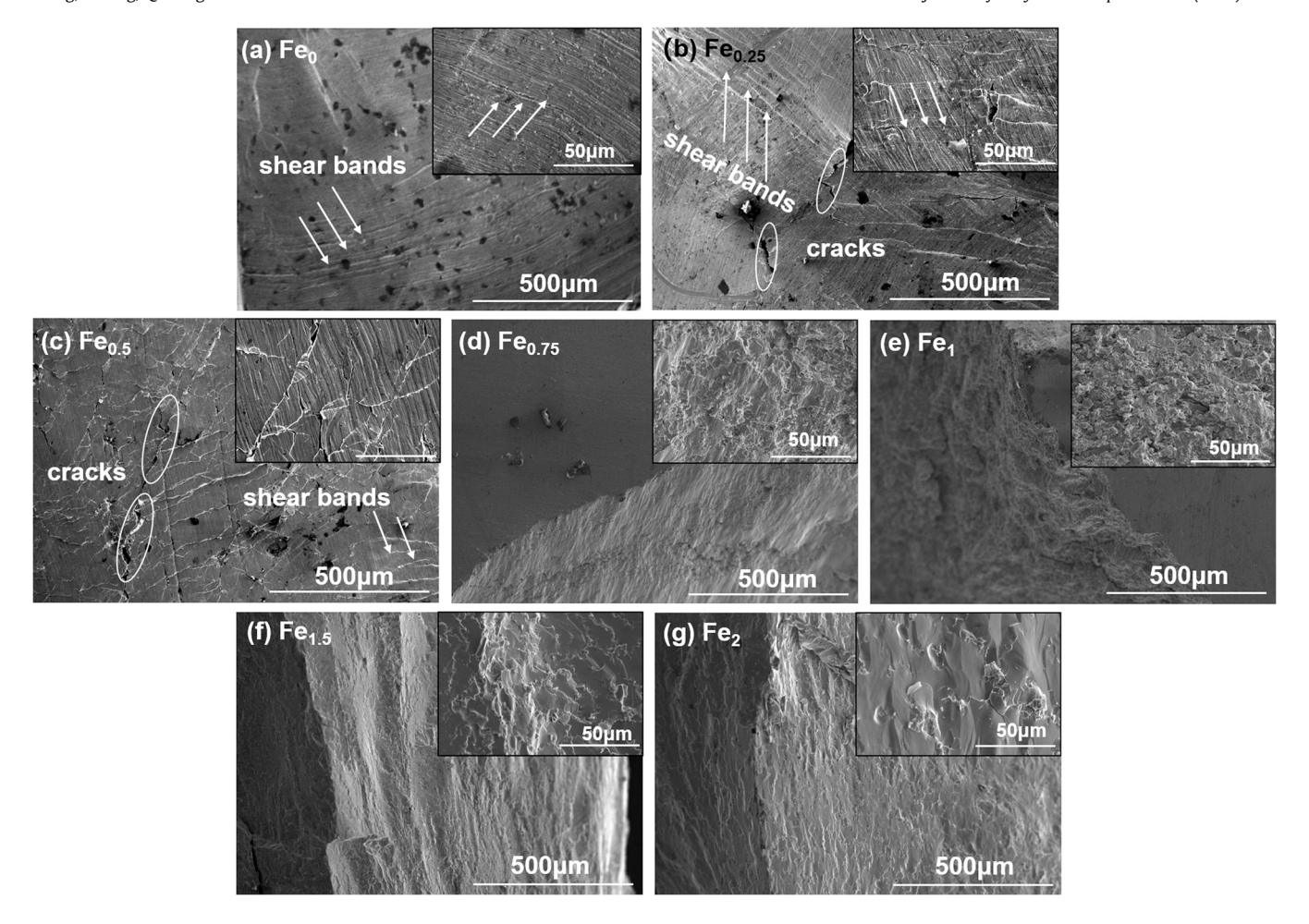


Fig. 6. SEM images of the surface morphologies for the Ti-Zr-Hf-Nb-Fe HEAs after the compressive deformation. The insets display their magnified morphologies.

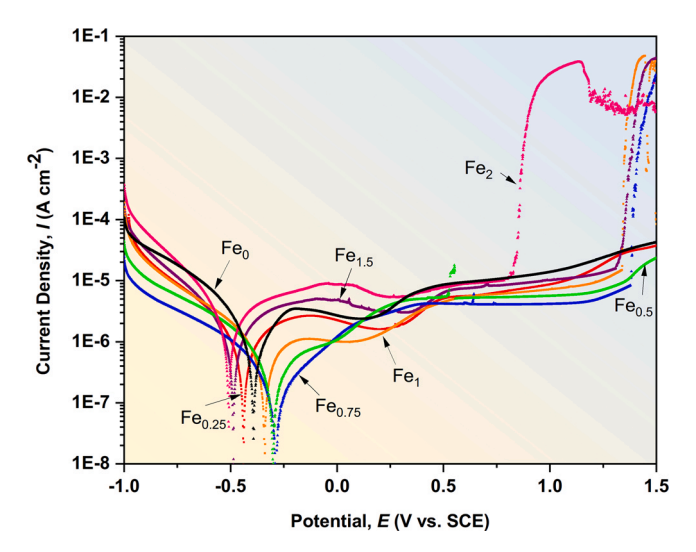


Fig. 7. Potentiodynamic-polarization curves of the Ti-Zr-Hf-Nb-Fe HEAs in the PBS solution

corrosion-current density ( $i_{\rm corr}$ ) of HEAs shows a declining trend from  $10.93 \times 10^{-7}~{\rm Acm^{-2}}$  for the Fe $_{0.}$  alloy to  $2.80 \times 10^{-7}~{\rm Acm^{-2}}$  for the Fe $_{0.5}$  alloy. Furthermore, no corrosion pitting, characterized by the notable increase in the current density, can be observed for the Fe $_{0.}$ Fe $_{0.25}$ , and Fe $_{0.5}$  alloys even at the high anode potential up to 1.5 V, demonstrating that the present Ti-Zr-Hf-Nb-Fe HEAs exhibit good pitting corrosion resistance provided that the Fe content does not

**Table 2** Electrochemical parameters of the Ti-Zr-Hf-Nb-Fe HEAs derived from potentiodynamic-polarization curves.

Alloys	E <sub>corr</sub> (V)	$i_{\rm corr} (10^{-7} \text{ A/cm}^2)$	$E_{\rm pit}$ (V)
Fe <sub>0</sub>	- 0.39 ± 0.03	10.93 ± 2.77	_
Fe <sub>0.25</sub>	$-0.42 \pm 0.05$	9.33 ± 1.61	-
Fe <sub>0.5</sub>	- 0.30 ± 0.01	$2.80 \pm 0.77$	-
Fe <sub>0.75</sub>	- 0.27 ± 0.01	1.66 ± 0.27	1.36 ± 0.02
Fe <sub>1</sub>	- 0.33 ± 0.02	5.18 ± 1.81	1.22 ± 0.12
Fe <sub>1.5</sub>	$-0.49 \pm 0.04$	15.5 ± 0.25	1.16 ± 0.16
Fe <sub>2</sub>	- 0.51 ± 0.01	27.1 ± 2.21	$0.82 \pm 0.03$

exceed 0.5. Significantly, the corrosion resistance of the Ti-Zr-Hf-Nb-Fe HEAs enhances with the increment of the Fe content ( $0 \le x \le 0.5$ ).

As the Fe content exceeds 1, further increasing the Fe content reduces the corrosion potential but increases the corrosion-current density of the alloys. Besides, pitting corrosion occurs for these alloys at high applied potentials, and the pitting-corrosion potentials ( $E_{\rm pit}$ ) decreases with the increase in the Fe content, implying the degradation of the pitting-corrosion resistance of the alloys. Among the Ti-Zr-Hf-Nb-Fe alloys, the Fe<sub>2</sub> alloy exhibits a pitting-corrosion potential at 0.82 V, and displays the lowest corrosion potential, the highest corrosion-current density, and the minimum passivation zone ( $\Delta E = E_{\rm pit} - E_{\rm corr}$ ), which corresponds to the worst corrosion resistance in the PBS solution. In contrast, the pitting corrosion of the Fe<sub>0.5</sub> alloy does not occur, and presents the great corrosion potential and low corrosion-current density. It can thus be assumed that the Fe<sub>0.5</sub> alloy exhibits the greatest corrosion resistance among the Ti-Zr-Hf-Nb-Fe alloys in the PBS solution.

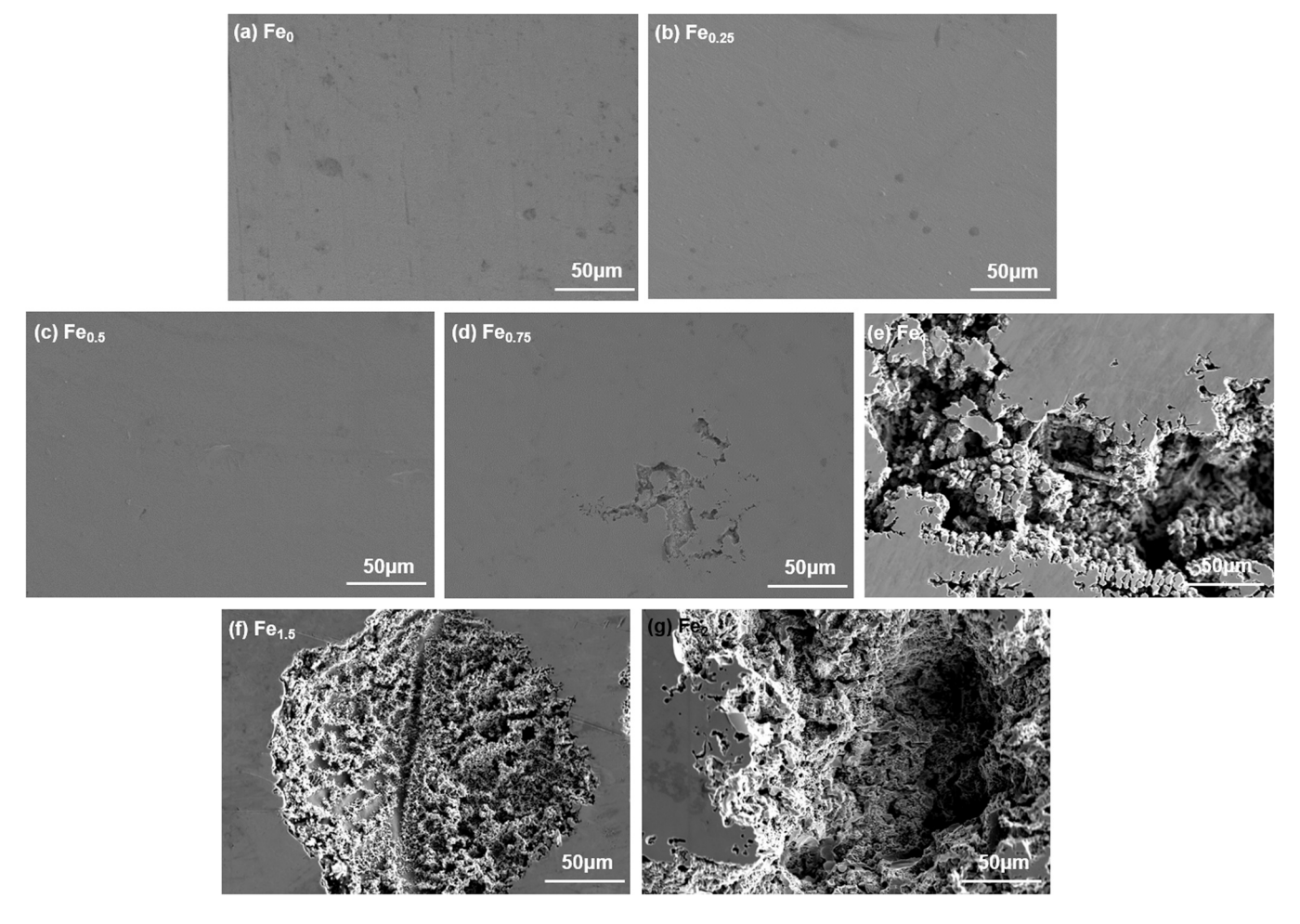


Fig. 8. SEM images of corrosion morphologies for the Ti-Zr-Hf-Nb-Fe HEAs after polarization experiments.

Fig. 8 presents the SEM images of corrosion morphologies for the Ti-Zr-Hf-Nb-Fe HEAs after polarization experiments. It is seen that the Fe<sub>0</sub>, Fe<sub>0.25</sub>, and Fe<sub>0.5</sub> alloys exhibit a smooth surface without the appearance of obvious corrosion pits, indicating that a dense passivation film has formed on their surfaces to resist the invasion of anions. Combined with the electrochemical parameters derived from the polarization curves, it is proved that adding a proper quantity of Fe to the HEAs can improves their corrosion resistance. However, starting from the Fe<sub>0.75</sub> alloy, shallow corrosion pits emerge on its surface after polarization. As the Fe content raises, the propagation of corrosion pits for the Fe<sub>1</sub> alloy takes place, and the width and depth of corrosion pits increase significantly, as illustrated in Fig. 8(e)–(f). The corrosion pits of the Fe<sub>1.5</sub> alloy are in the honeycomb shape and attached with a large amount of granular corrosion products. Furthermore, the surface of the Fe<sub>2</sub> alloy displays wider and deeper corrosion pits, indicating the graver corrosion. Therefore, increasing the fraction of Fe beyond 0.5 leads to the deterioration of the corrosion resistance in the Ti-Zr-Hf-Nb-Fe HEAs.

To further illustrate the reason for the good corrosion resistance of the Fe $_{0.5}$  alloy in the PBS solution, three alloys, including the Fe $_{0.5}$ , Fe $_{0.5}$ , and Fe $_{1}$  HEAs, were subjected to the XPS analysis. All samples were immersed in the PBS solution for 24 h before the experiment. The XPS full spectrum and narrow scanning spectra of the O, Ti, Zr, Hf, Nb, and Fe elements on the surfaces of the Ti-Zr-Hf-Nb-Fe HEAs are presented in Fig. 9, where "OX" represents the oxidized state and "metal" corresponds to the metallic state. Table 3 depicts the

distribution of elemental compositions on the surfaces of the HEAs from the XPS analysis.

From Fig. 9(a), the peaks of C 1s, O ls, Ti 2p, Zr 3d, Hf 4f, and Nb 3d can be detected in the XPS full spectrum for the Fe<sub>0</sub>, Fe<sub>0.5</sub>, and Fe<sub>1</sub> HEAs. On the surfaces of the Fe<sub>0.5</sub> and Fe<sub>1</sub> alloys, the Fe 2p peaks can also be seen. The C 1s peaks are caused by the inevitable carbon contamination. As we can see from the O 1s spectrum [Fig. 9(b)], the O element on the surface of the alloy is chiefly in forms of O<sup>2</sup>-, OH<sup>-</sup>, and bound water (H<sub>2</sub>O). The bound water can act as a substance used to trap dissolved metal ions and develop a thin film on the surface, preventing further corrosion [49]. The Ti 2p spectra of all three HEAs [Fig. 9(c)] are composed of Ti  $2p_{3/2}$  and Ti  $2p_{1/2}$  double peaks, corresponding to the TiO<sub>2</sub> (Ti<sup>4+</sup>) peak in the oxidized state. The peaks of Zr 3d in the Fig. 9(d) indicates the coexistence of Zr<sup>4+</sup> and Zr<sup>0</sup> in the surface film of the Fe<sub>0</sub> alloy, whereas the intensity of Zr<sup>0</sup> peaks is obviously reduced for  $\mathrm{Fe}_{0.5}$  and  $\mathrm{Fe}_1$  alloys. The Hf 4f spectrum in Fig. 9(e) illustrates the peaks corresponding to the Hf<sup>0</sup> and Hf<sup>4+</sup> states. Similarly, the peaks of Nb5+ and Nb0 can be observed in the Nb 3d spectrum of Fig. 9(f), where the intensities of Nb<sup>5+</sup> peaks for the  $Fe_{0.5}$  alloy are relatively higher than those of the other two alloys. Fig. 9(g) shows the Fe 2p spectra of the Fe<sub>0.5</sub> and Fe<sub>1</sub> alloys, showing the peaks corresponding to Fe<sup>3+</sup> and its satellite peaks, where a faint peak of Fe<sup>0</sup> is also detected on the Fe<sub>1</sub> alloy. Moreover, compared to the Fe<sub>0.5</sub> alloy, the intensity of the Fe<sup>3+</sup> peak of the Fe<sub>1</sub> alloy is substantially higher, demonstrating that more Fe oxides are generated on the surface of the Fe<sub>1</sub> alloy. It is noted that the primary

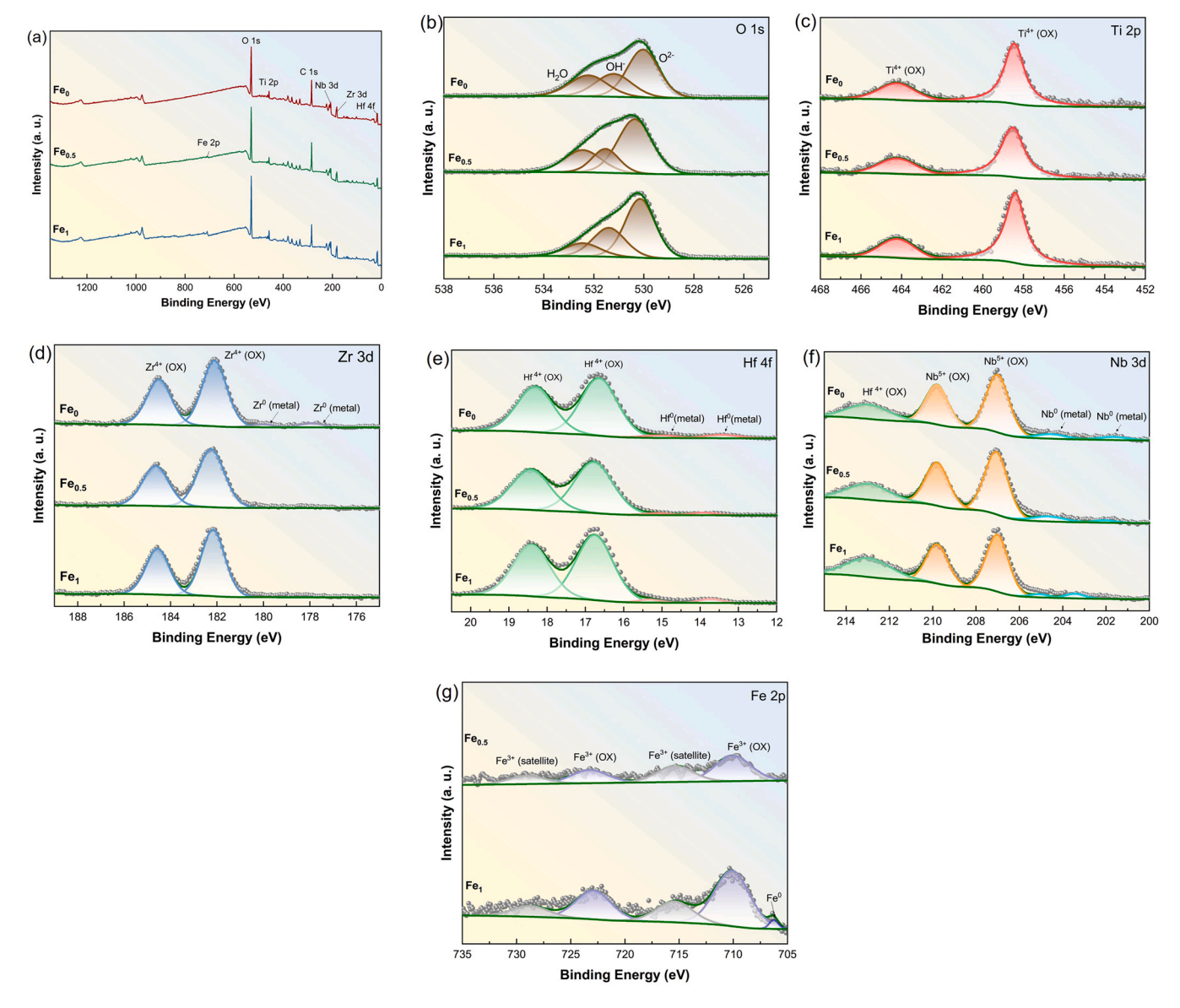


Fig. 9. (a) XPS full spectrum and narrow scanning spectra of the (b) O, (c) Ti, (d) Zr, (e) Hf, (f) Nb, and (g) Fe elements on the surfaces of the Ti-Zr-Hf-Nb-Fe HEAs.

**Table 3**XPS analysis results of the Ti-Zr-Hf-Nb-Fe HEAs after 24 h immersion in the PBS solution.

Elemental content (at%)		Fe <sub>0</sub>	Fe <sub>0.5</sub>	Fe <sub>1</sub>
O 1s	02-	31.39	38.02	34.94
	OH-	17.43	16.87	18.69
	H <sub>2</sub> O	16.56	13.12	9.19
Ti 2p	Ti <sup>4+</sup>	8.28	7.49	8.48
Zr 3d	$Zr^{4+}$	7.50	7.25	7.76
	$Zr^0$	0.93	_	_
Hf 4f	Hf <sup>4+</sup>	7.43	6.64	7.81
	Hf <sup>o</sup>	1.28	0.22	0.63
Nb 3d	Nb <sup>5+</sup>	6.24	6.82	6.30
	Nb <sup>o</sup>	2.22	0.28	0.44
Fe 2p	Fe <sup>3+</sup>	_	2.50	5.55
•	Fe <sup>0</sup>	=	_	0.21

oxides on the surfaces of the  $Fe_{0.5}$  and  $Fe_1$  alloys are  $TiO_2$ ,  $ZrO_2$ ,  $HfO_2$ ,  $Nb_2O_5$ , and  $Fe_2O_3$ , respectively.

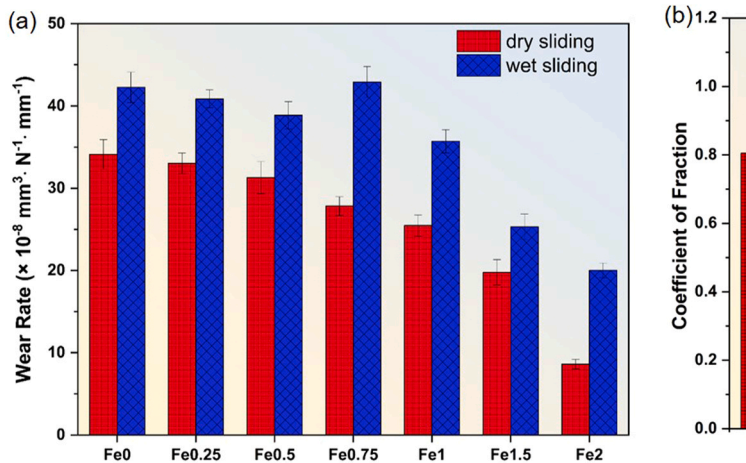
Table 3 shows that the fraction of O<sup>2-</sup> is the maximum for the Fe<sub>0.5</sub> alloy among the three alloys, implying that more oxidation

films occur on the  ${\rm Fe_{0.5}}$  alloy surface, which contributes to the high corrosion resistance.

#### 3.4. Tribological behavior of the HEAs

Fig. 10 exhibits the wear rates and frictional coefficients of the Ti-Zr-Hf-Nb-Fe HEAs under dry sliding (in air) and wet sliding (in the PBS solution) conditions. As shown in Fig. 10(a), the dry sliding wear rate of the Ti-Zr-Hf-Nb-Fe HEAs reduces from  $3.41 \times 10^7$  mm<sup>3</sup> N<sup>-1</sup> mm<sup>-1</sup> for the Fe<sub>0</sub> alloy to  $0.87 \times 10^7$  mm<sup>3</sup> N<sup>-1</sup> mm<sup>-1</sup> for the Fe<sub>2</sub> alloy with the increase in the Fe content. Apparently, the dry sliding wear rates of the HEAs tend to be inversely proportional to their hardness, which is consistent with the Archard's law [50].

The wet sliding-wear rates of the Fe $_0$  ~ Fe $_2$  alloys are  $4.23 \times 10^7$  mm $^3$  N $^{-1}$  mm $^{-1}$ ,  $4.09 \times 10^7$  mm $^3$  N $^{-1}$  mm $^{-1}$ ,  $3.87 \times 10^7$  mm $^3$  N $^{-1}$  mm $^{-1}$ ,  $4.29 \times 10^7$  mm $^3$  N $^{-1}$  mm $^{-1}$ ,  $3.58 \times 10^7$  mm $^3$  N $^{-1}$  mm $^{-1}$ ,  $2.53 \times 10^7$  mm $^3$  N $^{-1}$  mm $^{-1}$ , and  $2.01 \times 10^7$  mm $^3$  N $^{-1}$  mm $^{-1}$ , respectively. Obviously, the wet wear rates of the HEAs are larger than the dry sliding wear rates, indicating that the wear behavior of the HEAs is greatly reliant on the friction medium. Although the Fe $_{0.75}$  alloy presents the highest wet wear rate of  $4.29 \times 10^7$  mm $^3$  N $^{-1}$  mm $^{-1}$ ,



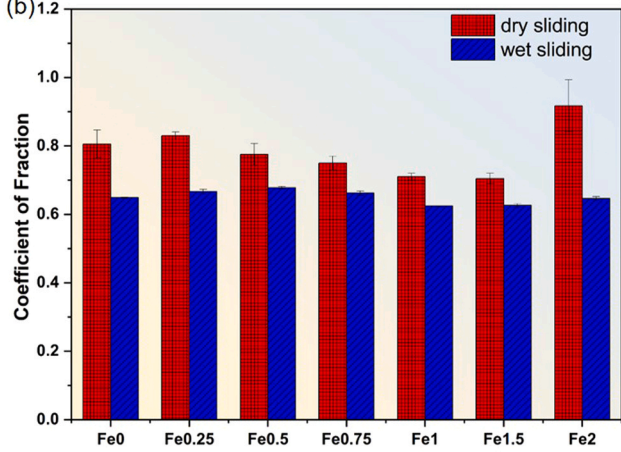


Fig. 10. (a) Wear rates and (b) coefficients of friction of the Ti-Zr-Hf-Nb-Fe HEAs under dry sliding during air and wet sliding in the PBS solution, respectively.

which is still less than that of  $4.60 \times 10^7$  mm<sup>3</sup> N<sup>-1</sup> mm<sup>-1</sup> for the Ti6Al4V alloy, according to the previous study [41].

Fig. 10(b) illustrates that the frictional coefficients of the Fe<sub>0</sub>  $\sim$  Fe<sub>2</sub> alloys in air are 0.81, 0.84, 0.79, 0.75, 0.71, 0.70, and 0.91, respectively. Meanwhile, the frictional coefficients of the Fe<sub>0</sub> ~ Fe<sub>2</sub> alloys under a wet sliding condition are 0.65, 0.67, 0.68, 0.66, 0.62, 0.63, and 0.65, respectively. The significant decrease in frictional coefficients under a wet sliding condition can be caused by the lubrication effect of the PBS solution, it is noteworthy that the Fe<sub>2</sub> alloy exhibits the lowest wear rate and the highest coefficient of friction under a dry sliding condition, which may result from its high hardness and brittleness, making the surface easily damaged and generating more abrasive chips during sliding. The coefficient of friction reflects the lubrication effect of the contact surface, and a high coefficient of friction indicates poor lubrication. The wear rate refers to the amount of wear on the material, and a high wear rate diminishes the service life of materials. Therefore, a high friction coefficient of the material does not necessarily imply a high wear rate.

Fig. 11(a)–(g) present the worn scar-surface morphologies of the Fe<sub>0</sub>-Fe<sub>2</sub> alloys under a dry sliding condition, respectively. It is observed that most of these alloys exist abrasive wear due to grooves parallel to the friction direction. The worn scar surfaces of the HEAs are composed of two typical zones with varying contrasts. The discrete island-like region displays a black contrast (as shown by white arrows), whereas the other zone exhibits a white contrast. Among the Ti-Zr-Hf-Nb-Fe HEAs, the Fe<sub>0.5</sub> alloy presents finely-spaced grooves with only a small amount of oxides adherence on the surface and a uniform distribution of plastic deformation without the formation of cracks. Moreover, the shallowing of grooves for the Fe<sub>1</sub> alloy is related to its higher hardness. Besides shallow grooves on the worn surface of the Fe<sub>1.5</sub> alloy, there are obvious material extrusion, fragmentation, and even spalling at the edge of the grooves, as shown in the white box of Fig. 11(f). The material spalling, corresponding to the typical fatigue-wear morphology, becomes more serious in the Fe<sub>2</sub> alloy [Fig. 11(g)], which may result from the low plasticity and high hardness of the alloy.

Fig. 12 exhibits the EDS results about different areas of the Ti-Zr-Hf-Nb-Fe HEAs under the dry sliding condition. We can indicate from the results that the black-contrast island-shaped regions are metallic oxides of alloying elements (including Ti, Zr, Hf, Nb, and Fe) with an average O content above 30 at%. On the worn surface of the Fe<sub>2</sub> alloy, the oxygen content exceeds 60 at%, denoting that the formation of surface layer with more oxides, which may be one of the reasons for the good wear resistance. Generally, the high-hardness oxide attachment may generate an elastic impulse effect on the

 $\rm Si_3N_4$  ball, and aggravate the damage to the ball. Furthermore, the exfoliated  $\rm Si_3N_4$  particles will scratch the fresh surface of alloys, producing the three-body wear and hastening alloys deterioration. However, if the metal is hard enough, it may exhibit a preventive effect on the further formation of grooves. During reciprocating friction, the continuous plastic deformation of the material can be inhibited, which initiates a sluggish effect on the wear of the materials to some extent. As a result, the wear resistance of the HEAs is enhanced [51], as displayed in Fig. 11(e). Apparently, with the increase in the Fe content, the wear mechanism of the HEAs in the air turns from the abrasive- and oxidation-wear for the Fe $_0$  to Fe $_1$  HEAs into the fatigue- and oxidation-wear for the Fe $_2$  alloys.

Fig. 13(a)-(g) demonstrate the worn scar-surface topographies for the Fe<sub>0</sub>-Fe<sub>2</sub> HEAs after wet sliding in the PBS solution, respectively. From Fig. 13(a)–(e), it can be seen that there are plow grooves and gray-contrast island-like convexity arranged in parallel to the sliding direction on the wear scars of the HEAs, which is similar to the abrasive wear-surface morphologies in the air [Fig. 11]. The EDSanalysis results of different regions on the Ti-Zr-Hf-Nb-Fe HEAs surface under the wet sliding condition are shown in Fig. 13. The high O content of the gray-contrast island-like convexity may be caused by the corrosion reaction during wet friction. For the Fe<sub>1.5</sub> [Fig. 13(f)] and Fe<sub>2</sub> [Fig. 13(g)] HEAs, the surface grooves are shallow, in addition to a small amount of gray black-contrast attachments. Moreover, there are a large number of pits, and the fraction of O in the pits is higher than that in other areas of the worn surface. This trend may be due to the fatigue wear of the alloy under applied loading, where the deformed layer of the alloy surface is exfoliated, and the exposed fresh metal surface reacts with the PBS solution. Thus, the wear mechanism shifts from the abrasive- and corrosivewear for the Fe<sub>0</sub> to Fe<sub>1</sub> alloys into the fatigue- and corrosive-wear for the Fe<sub>1.5</sub> and Fe<sub>2</sub> alloys after sliding in the PBS solution.

# 4. Discussion

Compared with conventional biomedical metallic materials, recently-developed Ti-Zr-Nb-based HEAs exhibit good comprehensive properties, including superior mechanical properties, high corrosion resistance, and excellent biocompatibility. For instance, the Hf<sub>25</sub>Nb<sub>25</sub>Ti<sub>25</sub>Zr<sub>25</sub> HEA shows a tensile yield strength of 879 MPa and a plastic strain of 14.9% [25]. Moreover, the TiNbTaZrMo HEA exhibits a yield strength exceeding 1000 MPa and good in vitro osteoblast biocompatibility comparable to that of a pure Ti [27]. Furthermore, Hua et al. [41] developed the Ti<sub>0.5</sub>ZrNbTaMo HEA displaying excellent wear and corrosion resistance by changing the content of Ti

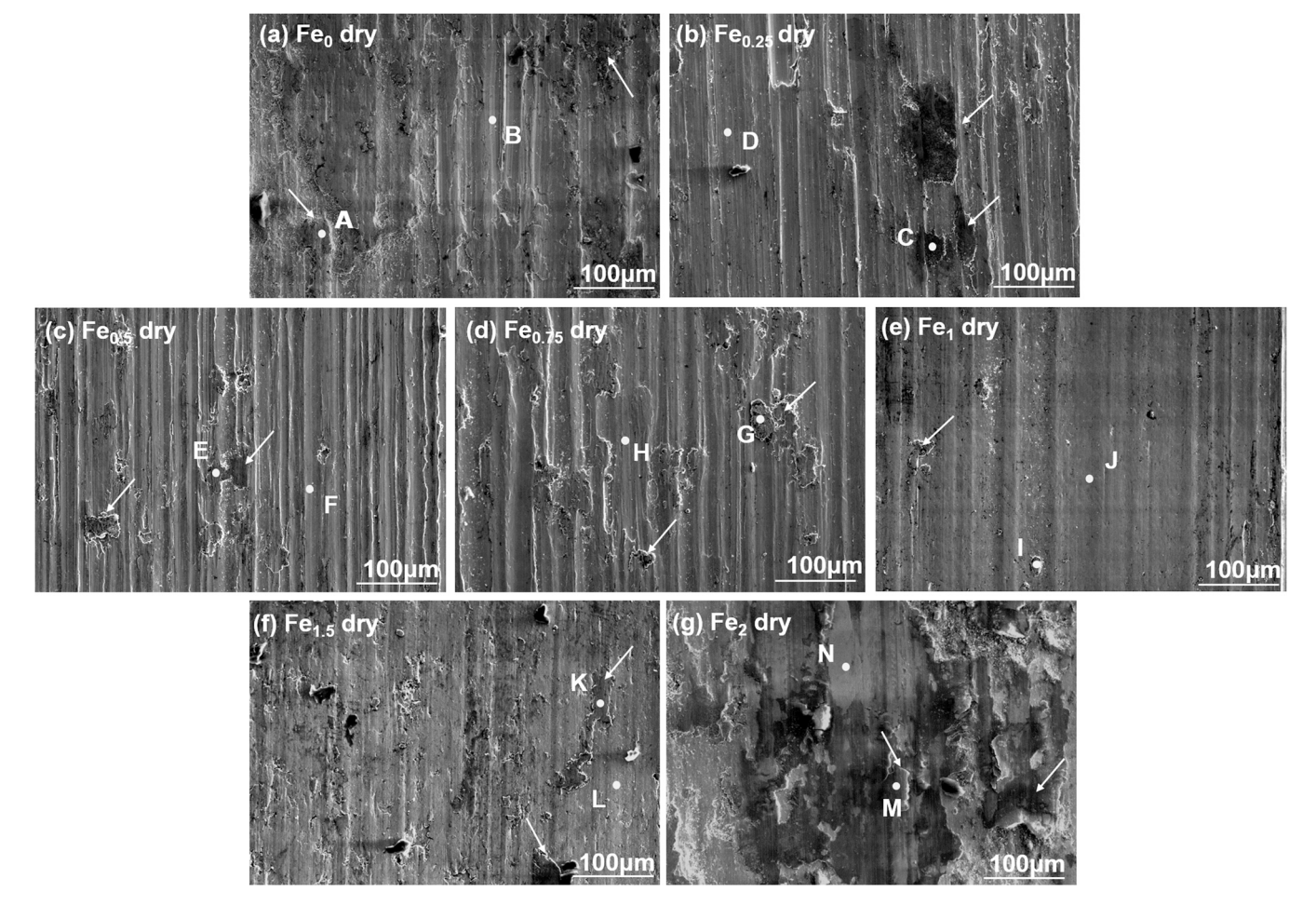
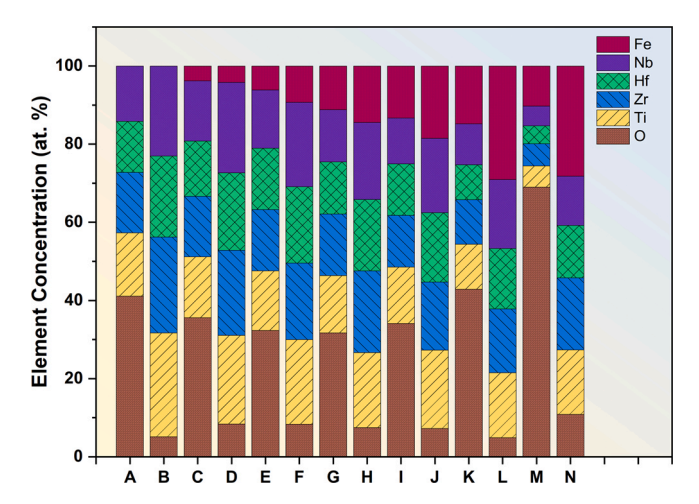


Fig. 11. SEM images of worn-scar surfaces of the Ti-Zr-Hf-Nb-Fe HEAs under the dry sliding condition.



**Fig. 12.** EDS analyses of different regions on the surfaces of the Ti-Zr-Hf-Nb-Fe HEAs under a dry sliding condition.

in the equiatomic TiZrNbTaMo HEAs. In the present study, we fabricated novel series of Ti-Zr-Hf-Nb-Fe refractory HEAs by adding the inexpensive Fe element into the TiZrHfNb HEA to modulate the microstructures and properties, and reduce the production cost. It is found that the TiZrHfNbFe<sub>0.5</sub> HEA presents a comparable plasticity and 1.5 times higher yield strength in comparison with those of the Ti6Al4V alloy. Besides, the corrosion and wear resistance of the Ti-Zr-Hf-Nb-Fe HEAs are better than those of the Ti6Al4V in the PBS solution. In addition, all of these constituent elements that we have

chosen are low biotoxic. Thus, the Ti-Zr-Hf-Nb-Fe HEAs present promising potential in the field of biomedical-implant materials.

## 4.1. Factors influencing the corrosion resistance of the HEAs

From Fig. 7 and Table 2, we can see that the corrosion-current densities of the Ti-Zr-Hf-Nb-Fe HEAs initially decrease and subsequently increase with the rising Fe content. Among those HEAs, although the corrosion current density of the Fe<sub>0.75</sub> alloy is the lowest, about  $1.66 \times 10^{-7} \text{A cm}^{-2}$ , pitting corrosion is seen on the Fe<sub>0.75</sub> alloy surface when polarized at a high applied voltage of 1.36 V. From Figs. 7 and 8, the Fe<sub>0.5</sub> alloy displays a low corrosion-current density of  $2.80 \times 10^{-7} \text{A cm}^{-2}$  and a high resistance to pitting corrosion even at the high applied voltage of 1.5 V. Accordingly, the Fe<sub>0.5</sub> alloy shows a better corrosion resistance than the Fe<sub>0.75</sub> alloy. Furthermore, further elevating the Fe content brings about the raise in the corrosion-current density, the decrease in the pitting potential, and a larger size of corrosion pits. Therefore, it can be considered that the Fe<sub>0.5</sub> alloy exhibits the best corrosion resistance of our study in the PBS solution. (Fig. 14).

According to the microstructure (Fig. 2) and compositional analysis (Fig. 3) results, the decrease in the corrosion resistance can be explained as follows:

(1) From the perspective of the alloy composition, Fe is enriched in the interdendrites, and Nb is enriched in the dendrites. It has been reported that the addition of the Nb element in the alloy facilitates enlarging the passivation zone [52], that is, the higher the Nb content, the better the corrosion resistance. Moreover,

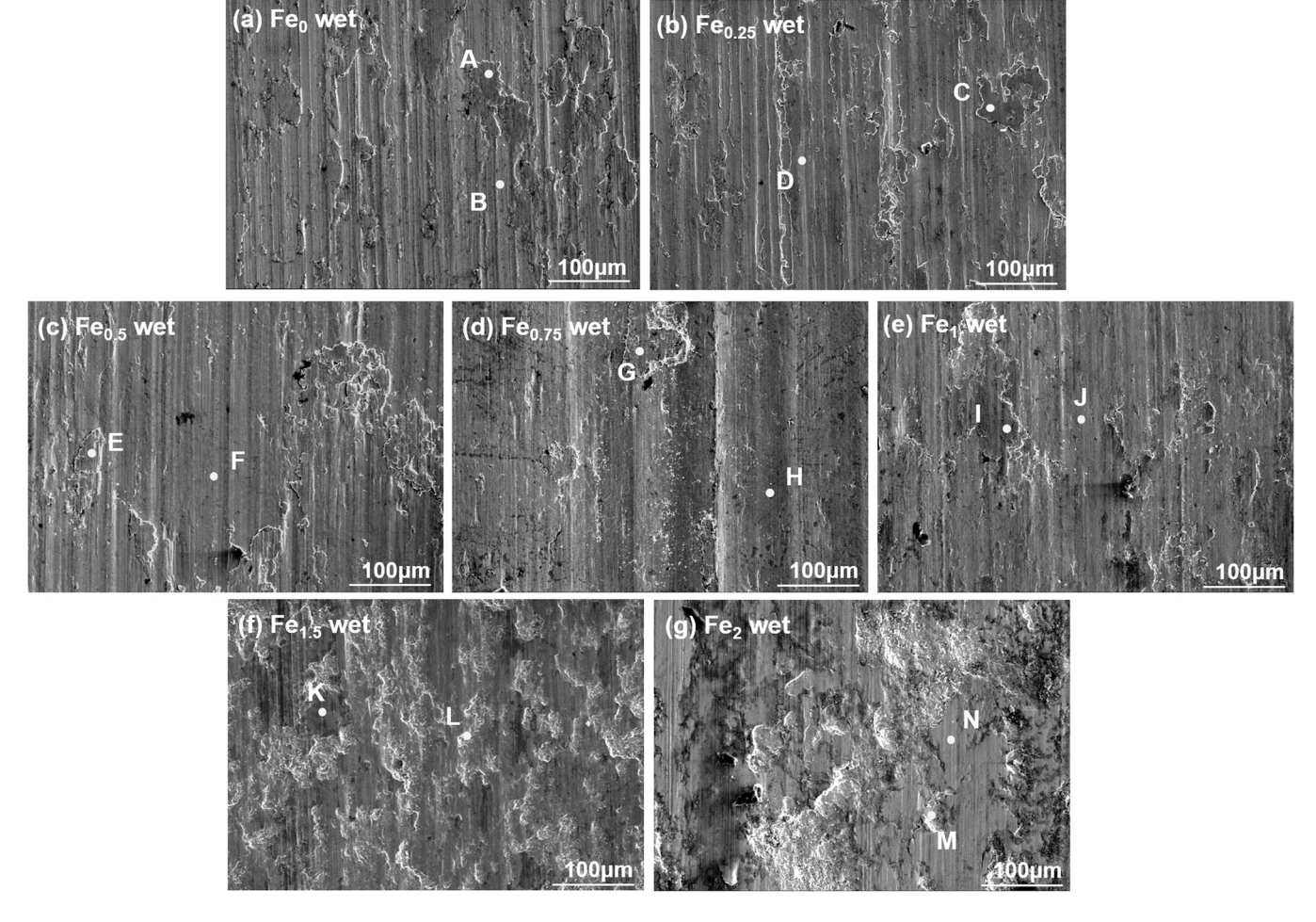
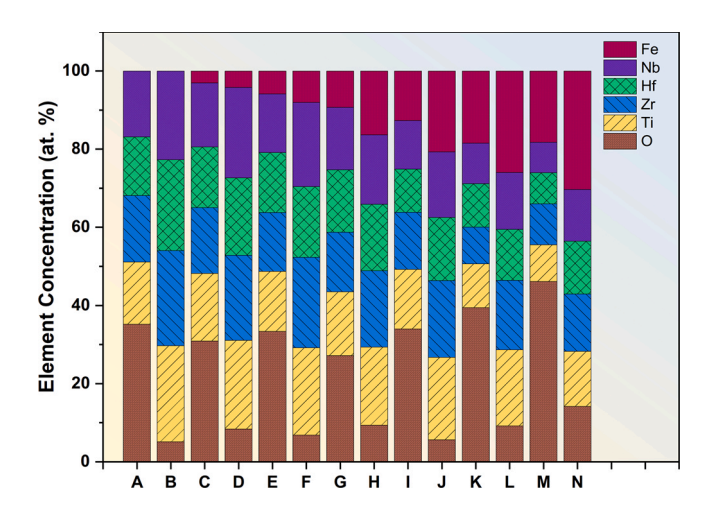


Fig. 13. SEM images of wear scars of the Ti-Zr-Hf-Nb-Fe HEAs under the wet wear condition.



**Fig. 14.** EDS analysis of different regions of the surfaces of Ti-Zr-Hf-Nb-Fe HEAs under the wet sliding condition.

the oxide/hydroxide of Fe is more porous and less stable than the oxides/hydroxides of Ti and Zr [53]. Hence, the protective film of interdendrites is weaker than that of the dendrites.

(2) From the perspective of microstructures of the HEAs, the appropriate amount of Fe alloying makes the dendrites become much finer and denser. According to the reported studies, grain refinement takes effects on the corrosion resistance of alloys

[54]. However, the influence results are not uniform, and there are conflicting conclusions even in the same alloy system [55]. In this study, with the increase in the Fe content, grain refinement occurs in the Fe<sub>0</sub>, Fe<sub>0.25</sub>, and Fe<sub>0.5</sub> alloys, and the number of active atoms of the material increases. Ti, Zr, Hf, and Nb are considered as corrosion-resistant elements, which can fast diffuse to the surface and form dense passivation films, thus improving the corrosion resistance of the HEAs. On the other hand, increasing the Fe content refers to the depletion of other constituent elements. When the contents of these corrosion-resistant elements are not sufficient to develop a compact protective films on the surface of the alloy, the preferred corrosion sites in grain boundaries make a great influence on the corrosion behavior. Owing to the inhomogeneous distribution of constituent elements, the galvanic corrosion takes place between the grains and grain boundaries, which can accelerate the corrosion rate. The reduction of the grain size brings about numerous grain boundaries, which behave as corrosion-prone areas. Thus, in this study, the Fe<sub>0.5</sub> alloy reaches an equilibrium state for the two competition factors and presents a superior corrosion performance.

The constituent elements of Ti, Zr, Hf, Nb, and Fe, exist mainly in two forms on the alloy surface. One is in the form of oxides constituting the surface-passivation film, such as TiO<sub>2</sub>, ZrO<sub>2</sub>, and Nb<sub>2</sub>O<sub>5</sub>, which have been shown to facilitate the formation of a continuous dense oxide film [37,38,41], and thus, slow down the corrosion of the alloy. The other is in the form of the metal state below the passivation film. It is seen from Table 3 that the Fe<sub>0.5</sub> alloy exhibits the

**Table 4**Electrochemical parameters of the relevant biomedical HEAs in simulated human solutions.

Alloys	Solution	$E_{\rm corr}\left(V\right)$	$i_{\rm corr}~({\rm A/cm^{-2}})$	$E_{\rm pit}$ (V)	Refs.
Ti <sub>20</sub> Zr <sub>20</sub> Nb <sub>20</sub> Ta <sub>20</sub> Mo <sub>20</sub>	PBS	- 0.61	~ 10 <sup>-6</sup>	-	[28]
TiZrTaHfNb	PBS	- 0.39	$7.2 \times 10^{-8}$	_	[36]
Ti <sub>1.5</sub> ZrTa <sub>0.5</sub> Hf <sub>0.5</sub> Nb <sub>0.5</sub>		- 0.39	$5.6 \times 10^{-7}$	=	
Ti <sub>20</sub> Zr <sub>20</sub> Hf <sub>20</sub> Nb <sub>20</sub> Ta <sub>20</sub>	Hank's	- 0.40	$8.0 \times 10^{-7}$	-	[37]
Ti <sub>0.5</sub> ZrNbTaMo	PBS	- 0.35	~ 10 <sup>-6</sup>	=	[41]
$Ti_{40}Mo_{15}V_{15}Cr_{15}Zr_{15}$	Ringer's	- 0.36	$7.12 \times 10^{-7}$	=	[59]
$Ti_{20}Mo_{20}V_{20}Cr_{20}Zr_{20}$	_	- 0.42	$3.08 \times 10^{-6}$	=	
(MoTa) <sub>0.2</sub> NbTiZr	PBS	- 0.53	~ 10 <sup>-6</sup>	=	[60]
TiZrNb	PBS	- 0.45	$5.61 \times 10^{-7}$	<del>-</del>	[61]
Ti <sub>45</sub> Zr <sub>45</sub> Nb <sub>10</sub>		-0.52	$5.76 \times 10^{-7}$	_	
TiZrHfNb	PBS	- 0.38	$1.08 \times 10^{-6}$	_	This work
TiZrHfNbFe <sub>0.5</sub>		- 0.30	$2.80 \times 10^{-7}$	-	

largest fraction of O (including O<sup>2-</sup>) among the three HEAs, which proves that more oxide films are generated on its surface to prevent the invasion of anions. Moreover, the fraction of Nb<sup>5+</sup> for the Fe<sub>0.5</sub> alloy is larger in the passivation film in comparison with that of the other two alloys. Previous studies have shown that the Nb element can expand the passivation zone of the alloy [52,56], and Nb is helpful in enhancing the corrosion resistance of the Ti-based alloys in Cl<sup>-</sup>-containing solutions [57,58]. The chemical reaction of the Nb element is described as follows [58]:

$$2Nb + 5H_2O = Nb_2O_5 + 10H^+ + 10e^-$$
 (7)

Furthermore, according to Macdonald's Point Defect Model (PDM), it has been discovered that the  $Nb^{5+}$  enhanced the quantity of  $O^{2-}$ , which counteracted the anionic vacancies in the passivation film, resulting in fewer film defects and hence, a more stable passivation film [58], Therefore, the  $Fe_{0.5}$  alloy exhibits the lower corrosion-current density and superior pitting resistance, compared with those of the  $Fe_0$  and  $Fe_1$  alloys.

Table 4 shows the comparison of the electrochemical parameters of the Ti-Zr-Hf-Nb-Fe HEAs with various biomedical HEAs in simulated physiological environments. It is worthy of noting that the present Fe $_{0.5}$  alloy possesses the highest corrosion potential and lower corrosion-current density, indicating the excellent corrosion resistance of the Fe $_{0.5}$  alloy in a simulated physiological solution.

#### 4.2. Factors influencing the wear resistance of the HEAs

As one of the conventional biomedical alloys, commercial pure Ti and some Ti alloys, are usually subjected to the "particle diseases" due to their poor wear resistance after implantation into the human body. Therefore, good wear resistance is proved to be one of the most important performance indicators of biomedical materials. The wear resistance of the present Ti-Zr-Hf-Nb-Fe HEAs is better than the Ti6Al4V alloy in both dry and wet-wear conditions, which can

**Table 5**Hardness and wear rate of some HEAs and Ti alloys.

Alloys	Couple-pair materials	Load (N)	Hardness (HV)	Wear rate (mm <sup>3</sup> N <sup>-1</sup> mm <sup>-1</sup> )	Refs.
Fe <sub>0.5</sub>	Si <sub>3</sub> N <sub>4</sub>	5	421.8	3.13 × 10 <sup>-7</sup>	This
Fe <sub>1</sub>			535.5	$2.55 \times 10^{-7}$	work
Fe <sub>1.5</sub>			665.3	$1.98 \times 10^{-7}$	
Fe <sub>2</sub>			767.3	$8.70 \times 10^{-8}$	
Ti6Al4V	$Si_3N_4$	5	320	$3.50 \times 10^{-7}$	[41]
TiZrNbTaMo			490	$2.91 \times 10^{-7}$	
Ti-20Zr-10Nb	TiN	1	235.2	$7.70 \times 10^{-7}$	[63]
Ti-30Zr			273.1	$6.40 \times 10^{-7}$	
CoCrFeMnNi	Si <sub>3</sub> N <sub>4</sub>	1	134.4	$7.40 \times 10^{-7}$	[64]
AlCoCrFeNi	Si <sub>3</sub> N <sub>4</sub>	3	522	$1.80 \times 10^{-7}$	[65]
MoTaWNbV	$Al_2O_3$	5	~ 773	$1.57 \times 10^{-4}$	[51]
Inconel 718			~ 300	$4.68 \times 10^{-4}$	[51]

help decrease the risk of "particle disease" resulting from wear debris. Thus, the HEAs are recently regarded as a promising candidate for orthopedic-implant materials.

Table 5 summarizes the hardness and wear rates of various HEA systems and Ti-based alloys. It can be seen that the MoTaWNb HEA shows a lower wear rate than that of Inconel 718 alloy when couple-pairing with the hard  $Al_2O_3$  ball owing to the high hardness of the MoTaWNb alloy. Under the dry-wear condition couple-pairing with  $Si_3N_4$  and TiN balls, the wear resistance shows an increasing trend with the increase in the hardness of alloys. For instance, the CoCr-FeMnNi alloy possesses the lowest hardness of 134.4 HV and thus, the highest wear rate of  $7.40 \times 10^{-7}$  mm<sup>3</sup> N<sup>-1</sup> mm<sup>-1</sup>. The Fe<sub>2</sub> alloy displays the highest hardness of 767.3 HV and lowest wear rate of  $8.70 \times 10^{-8}$  mm N<sup>-1</sup> mm<sup>-1</sup>. According to the Archard-wear model [50], the wear resistance strongly correlates with hardness: the higher the hardness, the better the wear resistance. The present wear and hardness results in Table 5 are consistent with the Archard's equation [50,62].

$$w = k \frac{NL}{H} \tag{8}$$

where the w, k, N, L and H are the wear volume, the proportionality constant, the normal load, the sliding distance and the hardness, respectively.

Previous studies also found that the hardness is not the only factor dominating the wear resistance of materials. For instance, Martin et al. investigated the wear behavior of the AlCoCrFeNiTi<sub>x</sub> HEAs with various Ti contents [66]. Although the hardness of the AlCoCrFeNiTi<sub>x</sub> HEAs increased with the Ti content, no apparent relation between the wear rate and hardness was found for those HEAs. The similar results were common in ceramic materials and amorphous alloys as well. Furthermore, it was suggested [67] that the fracture toughness plays an important role on the wear resistance as well. Increasing the fracture toughness of a material can improve its capacity to resist crack nucleation and propagation, contributing to the increased wear resistance. The wear resistance of the ductile metallic-crystalline materials is merely determined by their hardness. But for brittle ceramic or glass materials, the fracture toughness tends to be the main factor affecting the wear resistance.

Due to high entropy, sluggish diffusion and lattice distortion, the HEAs tend to form the simple face-centered-cubic (FCC), BCC, or HCP structures and special properties[68]. Generally, the HEAs with an FCC structure present better plasticity but lower strength and hardness among three structure alloys, whereas the BCC or HCP HEAs display higher hardness but lower plastic deformability than those of FCC HEAs [69]. In this study, the addition of the Fe element into the Ti-Zr-Hf-Nb HEA transforms the structure of the HEA from a BCC structure to BCC + HCP duplex structure, which remarkably increases the hardness of the alloys. Moreover, because the Fe element has a large radius difference with those of the other elements, the lattice distortion of the alloys is strongly exaggerated after the Fe

addition, which may increase the anti-slip properties of dislocations and thus, increase the wear resistance of alloys. The combined influence of both aspects results in a considerable increase in their wear resistance. However, since there are various experimental methods to evaluate the wear resistance of the HEAs, the published data on the friction and wear behavior is inadequate. Therefore, further investigations on the frictional-wear behavior and wear mechanism of the HEAs are required for their biomedical application.

#### 4.3. Potential of biomedical applications for the Ti-Zr-Hf-Nb-Fe HEAs

When we choose materials suitable for the biomedical application, biocompatibility is one of the most important performances, which refer to the capacity exhibiting no harmful effects on the host organism during service [70], for example, good stability during service, no harmful corrosion or abrasion products to the body, and similar properties to the replaced tissue. The Young's moduli of Ti6Al4V, 316L stainless steel, and CoCrMo alloys are about 110 GPa, 210 GPa, and 240 GPa, respectively, which are much higher than that of 10-40 GPa for the human bone [37]. Large modulus mismatches may result in inadequate loading of bone approximate to the implant materials, resulting in the "stress-shielding effect" [6,71]. Furthermore, corrosive wear usually takes place when metallic-implant materials work in the human body. This trend can generate wear particles accompanied by the release of toxic metal ions (e.g., Al, V, Ni ions, etc.), which results in the "particle diseases" and "aseptic loosening" [14,41]. To solve these problems, great attentions had been devoted to developing novel implant materials possessing good comprehensive mechanical properties, corrosion resistance, and biocompatibility.

Recently, refractory MEAs (medium-entropy alloys) and HEAs, such as Ti-Zr-Nb [61,72], Ti-Zr-Nb-Ta [26,73], Ti-Zr-Hf-Nb [25], Ti-Zr-Hf-Nb-Mo [31], Ti-Zr-Hf-Nb-Ta [30,36], Ti-Zr-Nb-Ta-Mo [28,74] and Ti-Zr-Hf-(Co)-Cr-Mo [75] have attracted much attention in the field of biomedical materials due to their good comprehensive properties and biocompatibility. Most of the refractory HEAs possess BCC structures and thus, generally display high yield strengths [28,30,31], and some of them even exhibit good plasticity [25,44]. It has been reported that Ti, Ta, Zr, Nb, and Hf show high biosafety and good biocompatibility [76,77]. For instance, Yang et al. [37] found that MC3T3-E1 cells exhibited as good cell adhesion, survival and proliferation behaviors on the surface of Ti<sub>20</sub>Zr<sub>20</sub>Hf<sub>20</sub>Nb<sub>20</sub>Ta<sub>20</sub> alloy as those of the Ti6Al4V alloy. Moreover, the non-equiatomic Ti<sub>40</sub>Zr<sub>20</sub>Hf<sub>10</sub>Nb<sub>20</sub>Ta<sub>10</sub> HEA also presented good proliferation for human gingival fibroblasts in comparison with that of the TiZrHf MEA [78]. The combination of good bio-corrosion resistance and in vitro biocompatibility of the Ti-Zr-Hf-Nb-Ta HEA indicates the promising potential of them for biomedical applications. Furthermore, Todai et al. [27] incubated osteoblasts on the surface of the Ti-Nb-Ta-Zr-Mo HEA, commercially pure titanium (CP-Ti), and 316L stainless steel for 24 h and found that the cells on the HEA and CP-Ti showed similar morphologies with a spreading pattern. Further analysis demonstrated that the cell density on the surface of the HEA was also significantly higher than that of the 316L stainless steel. Takao et al. [79] further modified the composition of the equimolar Ti-Nb-Ta-Zr-Mo biomedical HEA and found that the non-equiatomic Ti<sub>1.4</sub>Zr<sub>1.4</sub>Nb<sub>0.6</sub>Ta<sub>0.6</sub>Mo<sub>0.6</sub> alloy exhibited a higher amount of fibrous adhesion than that of the 316L stainless steel. Akmal et al. evaluated the in vivo biocompatibility of the (MoTa)<sub>0.2</sub>NbTiZr HEA [60] and found no abnormal neurological responses and toxicity during the implantation service.

Among the recently-developed refractory HEAs, such as Ti-Zr-Hf-Nb-Al [44], Ti-Zr-Hf-Nb-V[80], Ti-Zr-Hf-Al-V [81], Ti-Zr-Nb-Al-V [82] and Ti-Nb-Ta-Zr-W [73], the constituent elements, Al and V, are toxic

to the human body and can easily cause Alzheimer's disease, allergic reactions, and even cancer [83,84], which shows a potential danger of the long-term service in the human body. Moreover, the W element exhibits a high melting point (3695 K) and high raw material cost. Recently, Popescu et al. developed the Ti<sub>4</sub>Zr<sub>1.5</sub>Nb<sub>2.5</sub>TaFe biomedical HEA by adding Fe elements and found that it showed better corrosion resistance in Ringer's solution than that of the Ti6Al4V alloy [85]. Codescu et al. also prepared the FeMoTaTiZr refractory HEA and functionalized the alloy with an hydroxyapatite coating (HAP) to improve its biocompatibility, bioactivity, and corrosion resistance [86]. It is known that Fe is a necessary element of the human body and one of the main raw materials for hemoglobin. Moreover, Fe exhibits the lower melting point and raw material cost than those of noble elements, such as Mo, Ta, and W. Therefore, the addition of Fe can be considered as an effective strategy to achieve better biocompatibility and cost reduction of HEAs.

Thus, in this study, we selected five elements with low biological toxicity, Ti, Zr, Hf, Nb, and Fe, to develop a novel Ti-Zr-Hf-Nb-Fe HEA system, which not only reduces the raw material cost, but also ensures better comprehensive mechanical properties, corrosion resistance, and biocompatibility. Moreover, the Young's modulus of Fe<sub>0.5</sub> alloy is close to that of human bone, about 50 GPa, which is much lower than that of conventional implant materials, such as the Ti6Al4V alloy. The low Young's modulus of the Ti-Zr-Hf-Nb-Fe reduces the possibility of aseptic loosening for long-term implantation.

#### 5. Conclusion

In our study, a novel Ti-Zr-Hf-Nb-Fe system biomedical HEAs have been designed, and their microstructure, mechanical properties, corrosion and wear behaviors were investigated. The following are the primary conclusions:

- (1) The Ti-Zr-Hf-Nb-Fe HEAs show a dendritic structure consisting of BCC + Laves dual phases. The dendrites and interdendrites are mainly composed of BCC and Laves phases, respectively. With the increase in the Fe content, the dendrites become finer, and the volume fraction of the Laves phase raises.
- (2) The Vicker's microhardness of the Ti-Zr-Hf-Nb-Fe HEAs increases from 310 HV for the Fe<sub>0</sub> alloy to 770 HV for the Fe<sub>2</sub> alloy. The Fe<sub>0.5</sub> alloy exhibits good comprehensive mechanical properties with a high yield strength of 1450 MPa and a plastic strain of about 8%.
- (3) The corrosion-current density of the Ti-Zr-Hf-Nb-Fe HEAs initially decreases and subsequently raises with the increase in the Fe content. The Fe $_{0.5}$  alloy displays a high corrosion potential of  $-0.30\,\mathrm{V}$  and a low corrosion-current density of  $2.80\,\times\,10^{-7}\,\mathrm{A\,cm^{-2}}$ . Besides, after polarization, there are no corrosion pits visible for the Fe $_{0.5}$  alloy. It is demonstrated that the Fe $_{0.5}$  alloy possesses a relatively-higher passivation-film stability.
- (4) According to the XPS analyses, the surface films of the HEAs are mostly constituted of TiO<sub>2</sub>, ZrO<sub>2</sub>, HfO<sub>2</sub>, Nb<sub>2</sub>O<sub>5</sub>, and Fe<sub>2</sub>O<sub>3</sub>. The Fe<sub>0.5</sub> alloy displays the highest O<sup>2-</sup> and Nb<sup>5+</sup> contents, which contribute to the good corrosion resistance in the PBS solution.
- (5) Under the dry friction condition, the wear resistance of the Ti-Zr-Hf-Nb-Fe HEAs improves with the increase in the Fe content, which is attributed to the increased hardness. Although corrosive wear occurs for the Ti-Zr-Hf-Nb-Fe HEAs sliding in the PBS solution, the wet-wear resistance of the Ti-Zr-Hf-Nb-Fe HEAs is better than the Ti6Al4V alloy.
- (6) The good mechanical properties, high corrosion and wear resistance, the biocompatible constituent elements, as well as the low cost of the Fe addition render the Ti-Zr-Hf-Nb-Fe HEAs as promising candidates as biomedical-implantation materials.

#### CRediT authorship contribution statement

Wenjie Wang: Conceptualization, Methodology, Writing – original draft. Kaihuai Yang: Sample preparation, Data curation, Writing – review & editing. Qianting Wang: Investigation, Writing – review & editing. Pinqiang Dai: Investigation, Data curation, Writing – review & editing. Hui Fang: Investigation, Resources. Fangjuan Wu: Investigation, Resources. Qiaohang Guo: Investigation, Resources. Peter K Liaw: Writing – review & editing. Nengbin Hua: Conceptualization, Investigation, Writing – original draft, Writing – review & editing.

#### **Declaration of Competing Interest**

The authors declare that they have no known competing financial interests or personal relationships that could have appeared to influence the work reported in this paper.

#### Acknowledgement

The present work was supported by the Scientific Research Project of Fujian Provincial Department of Science and Technology (2021H0023, 2020I1009 and 2021L3015), the Scientific Research Project of Fujian University of Technology (GY-Z21032 and GY-Z20057), and Program for Innovative Research Team in Science and Technology in Fujian Province University. P.K.L. very much appreciates the supports from (1) the National Science Foundation DMR-1611180 and 1809640 with program directors, Drs. J. Yang, G. Shiflet, and D. Farkas and (2) the US Army Research Office Project nos. W911NF-13-1-0438 and W911NF-19-2-0049 with program managers, Drs. M.P. Bakas, S.N. Mathaudhu, and D.M. Stepp.

#### References

- T. Biswal, S.K. BadJena, D. Pradhan, Sustainable biomaterials and their applications: a short review, Mater. Today: Proc. 30 (2020) 274–282, https://doi.org/10. 1016/j.matpr.2020.01.437
- [2] C. Oses, C. Toher, S. Curtarolo, High-entropy ceramics, Nat. Rev. Mater. 5 (2020) 295–309, https://doi.org/10.1038/s41578-019-0170-8
- [3] J. Schroers, G. Kumar, T.M. Hodges, S. Chan, T.R. Kyriakides, Bulk metallic glasses for biomedical applications, JOM 61 (2009) 21–29, https://doi.org/10.1007/ s11837-009-0128-1
- [4] M.Z. Ibrahim, A.A.D. Sarhan, F. Yusuf, M. Hamdi, Biomedical materials and techniques to improve the tribological, mechanical and biomedical properties of orthopedic implants – a review article, J. Alloy. Compd. 714 (2017) 636–667, https://doi.org/10.1016/j.jallcom.2017.04.231
- [5] M. Geetha, A.K. Singh, R. Asokamani, A.K. Gogia, Ti based biomaterials, the ultimate choice for orthopaedic implants a review, Prog. Mater. Sci. 54 (2009) 397–425, https://doi.org/10.1016/j.pmatsci.2008.06.004
- [6] M. Long, H.J.B. Rack, Titanium alloys in total joint replacement—a materials science perspective, Biomaterials 19 (1998) 1621–1639, https://doi.org/10.1016/ S0142-9612(97)00146-4
- [7] A. Igual Muñoz, S. Mischler, Effect of the environment on wear ranking and corrosion of biomedical CoCrMo alloys, J. Mater. Sci.: Mater. Med. 22 (2011) 437–450, https://doi.org/10.1007/s10856-010-4224-0
- [8] M. Hussein, A. Mohammed, N. Al-Aqeeli, Wear characteristics of metallic biomaterials: a review, Materials 8 (2015) 2749–2768, https://doi.org/10.3390/ ma8052749
- [9] A. Chiba, K. Kumagai, N. Nomura, S. Miyakawa, Pin-on-disk wear behavior in a like-on-like configuration in a biological environment of high carbon cast and low carbon forged Co-29Cr-6Mo alloys, Acta Mater. 55 (2007) 1309-1318, https://doi.org/10.1016/j.actamat.2006.10.005
- [10] B. Cantor, I.T.H. Chang, P. Knight, A.J.B. Vincent, Microstructural development in equiatomic multicomponent alloys, Mater. Sci. Eng. A 375–377 (2004) 213–218, https://doi.org/10.1016/j.msea.2003.10.257
- [11] J.W. Yeh, S.K. Chen, S.J. Lin, J.Y. Gan, T.S. Chin, T.T. Shun, C.H. Tsau, S.Y. Chang, Nanostructured high-entropy alloys with multiple principal elements: novel alloy design concepts and outcomes, Adv. Eng. Mater. 6 (2004) 299–303, https:// doi.org/10.1002/adem.200300567
- [12] K.Y. Tsai, M.H. Tsai, J.W. Yeh, Sluggish diffusion in Co-Cr-Fe-Mn-Ni high-entropy alloys, Acta Mater. 61 (2013) 4887–4897, https://doi.org/10.1016/j.actamat.2013.04.058
- [13] J.W. Yeh, Physical metallurgy of high-entropy alloys, JOM 67 (2015) 2254–2261, https://doi.org/10.1007/s11837-015-1583-5
- [14] Y. Shi, B. Yang, P.K. Liaw, Corrosion-resistant high-entropy alloys: a review, Metals 7 (2017) 43, https://doi.org/10.3390/met7020043

- [15] H. Diao, X. Xie, F. Sun, K.A. Dahmen, P.K. Liaw, Mechanical properties of high-entropy alloys, High Entropy Alloy. (2016) 181–236, https://doi.org/10.1007/978-3-319-27013-5 6
- [16] M.A. Hemphill, T. Yuan, G.Y. Wang, J.W. Yeh, C.W. Tsai, A. Chuang, P.K. Liaw, Fatigue behavior of Al0.5CoCrCuFeNi high entropy alloys, Acta Mater. 60 (2012) 5723–5734, https://doi.org/10.1016/j.actamat.2012.06.046
- [17] W.-R. Wang, W.-L. Wang, J.-W. Yeh, Phases, microstructure and mechanical properties of AlxCoCrFeNi high-entropy alloys at elevated temperatures, J. Alloy. Compd. 589 (2014) 143–152, https://doi.org/10.1016/j.jallcom.2013.11.084
- [18] O.N. Senkov, G.B. Wilks, D.B. Miracle, C.P. Chuang, P.K. Liaw, Refractory high-entropy alloys, Intermetallics 18 (2010) 1758–1765, https://doi.org/10.1016/j.intermet.2010.05.014
- [19] A. Roh, D. Kim, S. Nam, D.-I. Kim, H.-Y. Kim, K.-A. Lee, H. Choi, J.-H. Kim, NbMoTaW refractory high entropy alloy composites strengthened by in-situ metal-non-metal compounds, J. Alloy. Compd. 822 (2020) 153423, https://doi. org/10.1016/j.jallcom.2019.153423
- [20] X. Zhu, X. Zhou, S. Yu, C. Wei, J. Xu, Y. Wang, Effects of annealing on the microstructure and magnetic property of the mechanically alloyed FeSiBAINiM (M=Co, Cu, Ag) amorphous high entropy alloys, J. Magn. Magn. Mater. 430 (2017) 59–64, https://doi.org/10.1016/j.jmmm.2017.01.028
- [21] Y. Lu, H. Jiang, S. Guo, T. Wang, Z. Cao, T. Li, A new strategy to design eutectic high-entropy alloys using mixing enthalpy, Intermetallics 91 (2017) 124–128, https://doi.org/10.1016/j.intermet.2017.09.001
- [22] Y. Lu, Y. Dong, H. Jiang, Z. Wang, Z. Cao, S. Guo, T. Wang, T. Li, P.K. Liaw, Promising properties and future trend of eutectic high entropy alloys, Scr. Mater. 187 (2020) 202–209, https://doi.org/10.1016/j.scriptamat.2020.06.022
- [23] P. Shi, R. Li, Y. Li, Y. Wen, Y. Zhong, W. Ren, Z. Shen, T. Zheng, J. Peng, X. Liang, Hierarchical crack buffering triples ductility in eutectic herringbone high-entropy alloys, Science 373 (2021) 912–918, https://doi.org/10.1126/science.abf6986
- [24] Z. Wang, Y. Yan, Y. Wu, X. Huang, Y. Zhang, Y. Su, L. Qiao, Corrosion and tribocorrosion behavior of equiatomic refractory medium entropy TiZr(Hf, Ta, Nb) alloys in chloride solutions, Corros. Sci. 199 (2022) 110166, https://doi.org/10. 1016/j.corsci.2022.110166
- [25] Y.D. Wu, Y.H. Cai, T. Wang, J.J. Si, J. Zhu, Y.D. Wang, X.D. Hui, A refractory Hf25Nb25Ti25Zr25 high-entropy alloy with excellent structural stability and tensile properties, Mater. Lett. 130 (2014) 277–280, https://doi.org/10.1016/j. matlet.2014.05.134
- [26] V.T. Nguyen, M. Qian, Z. Shi, T. Song, L. Huang, J. Zou, A novel quaternary equiatomic Ti-Zr-Nb-Ta medium entropy alloy (MEA), Intermetallics 101 (2018) 39–43, https://doi.org/10.1016/j.intermet.2018.07.008
- [27] M. Todai, T. Nagase, T. Hori, A. Matsugaki, A. Sekita, T. Nakano, Novel TiNbTaZrMo high-entropy alloys for metallic biomaterials, Scr. Mater. 129 (2017) 65–68, https://doi.org/10.1016/j.scriptamat.2016.10.028
- [28] S.P. Wang, J. Xu, TiZrNbTaMo high-entropy alloy designed for orthopedic implants: As-cast microstructure and mechanical properties, Mater. Sci. Eng. C 73 (2017) 80–89, https://doi.org/10.1016/j.msec.2016.12.057
- [29] O.N. Senkov, G.B. Wilks, J.M. Scott, D.B. Miracle, Mechanical properties of Nb25Mo25Ta25W25 and V20Nb20Mo20Ta20W20 refractory high entropy alloys, Intermetallics 19 (2011) 698–706, https://doi.org/10.1016/j.intermet.2011.01.004
- [30] Y. Yuan, Y. Wu, Z. Yang, X. Liang, Z. Lei, H. Huang, H. Wang, X. Liu, K. An, W. Wu, Z. Lu, Formation, structure and properties of biocompatible TiZrHfNbTa highentropy alloys, Mater. Res. Lett. 7 (2019) 225–231, https://doi.org/10.1080/21663831.2019.1584592
- [31] N.N. Guo, L. Wang, L.S. Luo, X.Z. Li, Y.Q. Su, J.J. Guo, H.Z. Fu, Microstructure and mechanical properties of refractory MoNbHfZrTi high-entropy alloy, Mater. Des. 81 (2015) 87–94, https://doi.org/10.1016/j.matdes.2015.05.019
- [32] X. Bao, T. Maimaitijuma, B. Yu, X. Li, G. Xi, S. Liu, Y. Cao, T. Zhang, Ti-Zr-Nb based BCC solid solution alloy containing trace Cu and Ag with low modulus and excellent antibacterial properties, Mater. Today Commun. 31 (2022) 103180, https://doi.org/10.1016/j.mtcomm.2022.103180
- [33] Q. Lu, X. Chen, W. Tian, H. Wang, P. Liu, H. Zhou, S. Fu, Y. Gao, M. Wan, X. Wang, Corrosion behavior of a non-equiatomic CoCrFeNiTi high-entropy alloy: a comparison with 304 stainless steel in simulated body fluids, J. Alloy. Compd. 897 (2022) 163036, https://doi.org/10.1016/j.jallcom.2021.163036
- [34] Y. Iijima, T. Nagase, A. Matsugaki, P. Wang, K. Ameyama, T. Nakano, Design and development of Ti-Zr-Hf-Nb-Ta-Mo high-entropy alloys for metallic biomaterials, Mater. Des. 202 (2021) 109548, https://doi.org/10.1016/j.matdes.2021. 109548
- [35] K. Glowka, M. Zubko, P. Swiec, K. Prusik, M. Szklarska, D. Chrobak, J.L. Labar, D. Stroz, Influence of molybdenum on the microstructure, mechanical properties and corrosion resistance of Ti20Ta20Nb20(ZrHf)20-xMox (Where: x = 0, 5, 10, 15, 20) high entropy alloys, Materials 15 (2022) 393, https://doi.org/10.3390/ps.15010232
- [36] A. Motallebzadeh, N.S. Peighambardoust, S. Sheikh, H. Murakami, S. Guo, D. Canadinc, Microstructural, mechanical and electrochemical characterization of TiZrTaHfNb and Ti1.5ZrTa0.5Hf0.5Nb0.5 refractory high-entropy alloys for biomedical applications, Intermetallics 113 (2019) 106572, https://doi.org/10.1016/i.intermet.2019.106572
- [37] W. Yang, Y. Liu, S. Pang, P.K. Liaw, T. Zhang, Bio-corrosion behavior and in vitro biocompatibility of equimolar TiZrHfNbTa high-entropy alloy, Intermetallics 124 (2020) 106845, https://doi.org/10.1016/j.intermet.2020.106845
- [38] Q. Zhou, S. Sheikh, P. Ou, D. Chen, Q. Hu, S. Guo, Corrosion behavior of Hf0.5Nb0.5Ta0.5Ti1.5Zr refractory high-entropy in aqueous chloride solutions, Electrochem. Commun. 98 (2019) 63–68, https://doi.org/10.1016/j.elecom.2018. 11.009

- [39] W. Yang, S. Pang, Y. Liu, Q. Wang, P.K. Liaw, T. Zhang, Design and properties of novel Ti-Zr-Hf-Nb-Ta high-entropy alloys for biomedical applications, Intermetallics 141 (2022) 107421, https://doi.org/10.1016/j.intermet.2021.107421
- [40] S. Gurel, A. Nazarahari, D. Canadinc, H. Cabuk, B. Bal, Assessment of bio-compatibility of novel TiTaHf-based high entropy alloys for utility in orthopedic implants, Mater. Chem. Phys. 266 (2021) 124573, https://doi.org/10.1016/j.matchemphys.2021.124573
- [41] N. Hua, W. Wang, Q. Wang, Y. Ye, S. Lin, L. Zhang, Q. Guo, J. Brechtl, P.K. Liaw, Mechanical, corrosion, and wear properties of biomedical Ti–Zr–Nb–Ta–Mo high entropy alloys, J. Alloy. Compd. 861 (2021) 157997, https://doi.org/10.1016/j. iallcom.2020.157997
- [42] Y. Zhang, Y.J. Zhou, J.P. Lin, G.L. Chen, P.K. Liaw, Solid-solution phase formation rules for multi-component alloys, Adv. Eng. Mater. 10 (2008) 534–538, https:// doi.org/10.1002/adem.200700240
- [43] X. Yang, Y. Zhang, Prediction of high-entropy stabilized solid-solution in multi-component alloys, Mater. Chem. Phys. 132 (2012) 233–238, https://doi.org/10.1016/j.matchemphys.2011.11.021
- [44] V. Bhardwaj, Q. Zhou, F. Zhang, W. Han, Y. Du, K. Hua, H. Wang, Effect of Al addition on the microstructure, mechanical and wear properties of TiZrNbHf refractory high entropy alloys, Tribol. Int. 160 (2021) 107031, https://doi.org/10.1016/j.tribojnt.2021.107031
- [45] C. Mathiou, A. Poulia, E. Georgatis, A.E. Karantzalis, Microstructural features and dry - sliding wear response of MoTaNbZrTi high entropy alloy, Mater. Chem. Phys. 210 (2018) 126–135, https://doi.org/10.1016/j.matchemphys.2017.08.036
- [46] G. He, J. Eckert, W. Löser, M. Hagiwara, Composition dependence of the microstructure and the mechanical properties of nano/ultrafine-structured Ti-Cu-Ni-Sn-Nb alloys, Acta Mater. 52 (2004) 3035-3046, https://doi.org/10. 1016/i.actamat.2004.03.006
- [47] B. Ren, Z.X. Liu, D.M. Li, L. Shi, B. Cai, M.X. Wang, Corrosion behavior of CuCrFeNiMn high entropy alloy system in 1 M sulfuric acid solution, Mater. Corros. 63 (2012) 828–834, https://doi.org/10.1002/maco.201106072
- [48] N. Kumar, M. Fusco, M. Komarasamy, R. Mishra, M. Bourham, K. Murty, Understanding effect of 3.5 wt% NaCl on the corrosion of AlO. 1CoCrFeNi highentropy alloy, J. Nucl. Mater. 495 (2017) 154–163, https://doi.org/10.1016/j. inucrnat 2017 08 015
- [49] G. Okamoto, Passive film of 18-8 stainless steel structure and its function, Corros. Sci. 13 (1973) 471–489, https://doi.org/10.1016/0010-938X(73)90031-0
- [50] J.F. Archard, Contact and rubbing of flat surfaces, J. Appl. Phys. 24 (1953) 981–988, https://doi.org/10.1063/1.1721448
- [51] A. Poulia, E. Georgatis, A. Lekatou, A.E. Karantzalis, Microstructure and wear behavior of a refractory high entropy alloy, Int. J. Refract. Met. Hard Mater. 57 (2016) 50–63, https://doi.org/10.1016/j.ijrmhm.2016.02.006
  [52] M. Zhang, L. Zhang, P.K. Liaw, G. Li, R. Liu, Effect of Nb content on thermal stability,
- [52] M. Zhang, L. Zhang, P.K. Liaw, G. Li, R. Liu, Effect of Nb content on thermal stability, mechanical and corrosion behaviors of hypoeutectic CoCrFeNiNbχ high-entropy alloys, J. Mater. Res. 33 (2018) 3276–3286, https://doi.org/10.1557/jmr.2018.103
- [53] X. Shang, Z. Wang, F. He, J. Wang, J. Li, J. Yu, The intrinsic mechanism of corrosion resistance for FCC high entropy alloys, Sci. China: Technol. Sci. 61 (2017) 189–196, https://doi.org/10.1007/s11431-017-9114-1
- [54] S.C. Tjong, H. Chen, Nanocrystalline materials and coatings, Mater. Sci. Eng. R. 45 (2004) 1–88, https://doi.org/10.1016/j.mser.2004.07.001
- [55] K. Ralston, N.J.C. Birbilis, Effect of grain size on corrosion: a review, Corrosion 66 (2010), https://doi.org/10.5006/1.3462912
- [56] C.H. Tsau, C.Y. Yeh, M.C. Tsai, The effect of Nb-content on the microstructures and corrosion properties of CrFeCoNiNbx high-entropy alloys, Materials 12 (2019), https://doi.org/10.2300/pp.12222716
- [57] Y.Y. Steven, J.R. Scully, C.M. Vitus, Influence of niobium and zirconium alloying additions on the anodic dissolution behavior of activated titanium in HCl solutions, J. Electrochem. Soc. 148 (2001) B68, https://doi.org/10.1149/1.1337605
- [58] M. Metikos-Huković, A. Kwokal, J. Piljac, The influence of niobium and vanadium on passivity of titanium-based implants in physiological solution, Biomaterials 24 (2003) 3765–3775, https://doi.org/10.1016/S0142-9612(03)00252-7
- [59] H. Song, S. Lee, K. Lee, Microstructure and electrochemical behaviors of equiatomic TiMoVCrZr and Ti-rich TiMoVCrZr high-entropy alloys for metallic biomaterials, Arch. Metall. Mater. 65 (2020) 1317–1322, https://doi.org/10.24425/amm.2020.133692
- [60] M. Akmal, A. Hussain, M. Afzal, Y.I. Lee, H.J. Ryu, Systematic study of (MoTa) NbTiZr medium- and high-entropy alloys for biomedical implants- In vivo biocompatibility examination, J. Mater. Sci. Technol. 78 (2021) 183–191, https://doi. org/10.1016/j.jimst.2020.10.049
- [61] S. Hu, T. Li, Z. Su, D. Liu, Research on suitable strength, elastic modulus and abrasion resistance of Ti–Zr–Nb medium entropy alloys (MEAs) for implant adaptation, Intermetallics 140 (2022) 107401, https://doi.org/10.1016/j.intermet.2021.107401
- [62] M. R, P. Bellon, R.S. Averback, Wear resistance of Cu/Ag multilayers: a microscopic study, ACS Appl. Mater. Interfaces 10 (2018) 15288–15297, https://doi.org/10.1021/acsami.8b03015
- [63] W.-T. Qu, X.-G. Sun, B.-F. Yuan, K.-M. Li, Z.-G. Wang, Y. Li, Tribological behaviour of biomedical Ti–Zr-based shape memory alloys, Rare Met. 36 (2017) 478–484, https://doi.org/10.1007/s12598-017-0882-0

- [64] A. Ayyagari, C. Barthelemy, B. Gwalani, R. Banerjee, T.W. Scharf, S. Mukherjee, Reciprocating sliding wear behavior of high entropy alloys in dry and marine environments, Mater. Chem. Phys. 210 (2018) 162–169, https://doi.org/10.1016/j. matchemphys. 2017.07.031
- [65] Y. Wang, Y. Yang, H. Yang, M. Zhang, S. Ma, J. Qiao, Microstructure and wear properties of nitrided AlCoCrFeNi high-entropy alloy, Mater. Chem. Phys. 210 (2018) 233–239, https://doi.org/10.1016/j.matchemphys.2017.05.029
- [66] M. Lobel, T. Lindner, T. Mehner, T. Lampke, Influence of titanium on microstructure, phase formation and wear behaviour of AlCoCrFeNiTix high-entropy alloy, Entropy 20 (2018) 505, https://doi.org/10.3390/e20070505
- [67] N. Hua, X. Zhang, Z. Liao, X. Hong, Q. Guo, Y. Huang, X. Ye, W. Chen, T. Zhang, X. Jin, Dry wear behavior and mechanism of a Fe-based bulk metallic glass: description by Hertzian contact calculation and finite-element method simulation, J. Non-Cryst. Solids 543 (2020) 120065, https://doi.org/10.1016/j.jnoncrysol.2020.120065
- [68] Q. Ding, Y. Zhang, X. Chen, X. Fu, D. Chen, S. Chen, L. Gu, F. Wei, H. Bei, Y. Gao, M. Wen, J. Li, Z. Zhang, T. Zhu, R.O. Ritchie, Q. Yu, Tuning element distribution, structure and properties by composition in high-entropy alloys, Nature 574 (2019) 223–227, https://doi.org/10.1038/s41586-019-1617-1
- [69] Y. Zhang, T.T. Zuo, Z. Tang, M.C. Gao, K.A. Dahmen, P.K. Liaw, Z.P. Lu, Microstructures and properties of high-entropy alloys, Prog. Mater. Sci. 61 (2014) 1–93, https://doi.org/10.1016/j.pmatsci.2013.10.001
- [70] L.L. Hench, J.M. Polak, Third-generation biomedical materials, Science 295 (2002) 1014–1017, https://doi.org/10.1126/science.1067404
- [71] B. Lin, K. Yang, X. Bao, J. Liu, Q. Guo, L. Zhang, Q. Wang, N. Hua, Enhanced wear, corrosion, and corrosive-wear resistance of the biocompatible Ti-based bulk metallic glass by oxidation treatment, J. Non-Cryst. Solids 576 (2022) 121231, https://doi.org/10.1016/j.jnoncrysol.2021.121231
- [72] S. Hu, T. Li, Z. Su, S. Meng, Z. Jia, D. Liu, A novel TiZrNb medium entropy alloy (MEA) with appropriate elastic modulus for biocompatible materials, Mater. Sci. Eng. B 270 (2021) 115226, https://doi.org/10.1016/j.mseb.2021.115226
- [73] T. Nagase, K. Mizuuchi, T. Nakano, Solidification microstructures of the ingots obtained by arc melting and cold crucible levitation melting in TiNbTaZr MEdium-entropy Alloy and TiNbTaZrX (X = V, Mo, W) high-entropy alloys, Entropy 21 (2019) 483, https://doi.org/10.3390/e21050483
- [74] C. Li, Y. Ma, X. Yang, M. Hou, New TiTaNbZrMo high-entropy alloys for metallic biomaterials, Mater. Res. Express 8 (2021) 105403, https://doi.org/10.1088/2053-1591/ac2f0b
- [75] T. Nagase, Y. Iijima, A. Matsugaki, K. Ameyama, T. Nakano, Design and fabrication of Ti-Zr-Hf-Cr-Mo and Ti-Zr-Hf-Co-Cr-Mo high-entropy alloys as metallic biomaterials, Mater. Sci. Eng. C 107 (2020) 110322, https://doi.org/10.1016/j.msec. 2019.110322
- [76] M. Calin, A. Gebert, A.C. Ghinea, P.F. Gostin, S. Abdi, C. Mickel, J. Eckert, Designing biocompatible Ti-based metallic glasses for implant applications, Mater. Sci. Eng. C 33 (2013) 875–883, https://doi.org/10.1016/j.msec.2012.11.015
- [77] H. Matsuno, A. Yokoyama, F. Watari, M. Uo, T. Kawasaki, Biocompatibility and osteogenesis of refractory metal implants, titanium, hafnium, niobium, tantalum and rhenium, Biomaterials 22 (2001) 1253–1262, https://doi.org/10.1016/S0142-9612(00)00275.1
- [78] S. Wang, D. Wu, H. She, M. Wu, D. Shu, A. Dong, H. Lai, B. Sun, Design of high-ductile medium entropy alloys for dental implants, Mater. Sci. Eng., C 113 (2020) 110959, https://doi.org/10.1016/j.msec.2020.110959
- [79] T. Hori, T. Nagase, M. Todai, A. Matsugaki, T. Nakano, Development of non-equiatomic Ti-Nb-Ta-Zr-Mo high-entropy alloys for metallic biomaterials, Scr. Mater. 172 (2019) 83–87, https://doi.org/10.1016/j.scriptamat.2019.07.011
- [80] M. Feuerbacher, T. Lienig, C. Thomas, A single-phase bcc high-entropy alloy in the refractory Zr-Nb-Ti-V-Hf system, Scr. Mater. 152 (2018) 40–43, https://doi. org/10.1016/j.scriptamat.2018.04.009
- [81] T. Nagase, M. Todai, P. Wang, S.H. Sun, T. Nakano, Design and development of (Ti, Zr, Hf)-Al based medium entropy alloys and high entropy alloys, Mater. Chem. Phys. 276 (2022) 125409, https://doi.org/10.1016/j.matchemphys.2021.125409
- [82] R. Huang, J. Tan, W. Li, Q. Dong, C.J. Li, X.M. Qin, S.F. Guo, Y.P. Lu, Effects of V content on the microstructure and mechanical properties of Nb31Ti37-Zr26Al6V refractory medium-entropy alloys, Intermetallics 143 (2022) 107472, https://doi.org/10.1016/j.intermet.2022.107472
- [83] M. Niinomi, Recent metallic materials for biomedical applications, Metall. Mater. Trans. A 33 (2002) 477–486, https://doi.org/10.1007/s11661-002-0109-2
- [84] A. Yamamoto, R. Honma, M. Sumita, Cytotoxicity evaluation of 43 metal salts using murine fibroblasts and osteoblastic cells, J. Biomed. Mater. Res. 39 (1998) 331–340, https://doi.org/10.1002/(SICI)1097-4636(199802)39:2<331::AID-IBM22>3.0.CO:2-F.
- [85] G. Popescu, B. Ghiban, C.A. Popescu, L. Rosu, R. Truscă, I. Carcea, V. Soare, D. Dumitrescu, I. Constantin, M.T. Olaru, B.A. Carlan, New TiZrNbTaFe high entropy alloy used for medical applications, IOP Conf. Ser.: Mater. Sci. Eng. 400 (2018) 022049, https://doi.org/10.1088/1757-899x/400/2/022049
- [86] M.M. Codescu, A. Vladescu, V. Geanta, I. Voiculescu, I. Pana, M. Dinu, A.E. Kiss, V. Braic, D. Patroi, V.E. Marinescu, Bio-functionalization of a novel biocompatible high entropy alloy used for bone implants, Preprints (2021), https://doi.org/10.20944/preprints202104.0259.v1 (2021040259).